# INVERSION OF GRAVITY DATA FOR DEPTH-TO-BASEMENT ESTIMATE USING THE VOLUME AND SURFACE INTEGRAL METHODS: MODEL AND CASE STUDY

by

Baris Dadak

A thesis submitted to the faculty of
The University of Utah
in partial fulfillment of the requirements for the degree of

Master of Science

in

Geophysics

Department of Geology and Geophysics

The University of Utah

May 2017

**The University of Utah Graduate School**

# STATEMENT OF THESIS APPROVAL

The thesis of Baris Dadak

has been approved by the following supervisory committee members:

| | | |
|---|---|---|
| Michael S. Zhdanov | , Chair | 07/29/2016<br>Date Approved |
| Le Wan | , Member | 07/29/2016<br>Date Approved |
| Erich U. Petersen | , Member | 07/29/2016<br>Date Approved |

and by Thure E. Cerling , Chair/Dean of

the Department/College/School of Geology and Geophysics

and by David B. Kieda, Dean of The Graduate School.

# ABSTRACT

In this thesis, I applied Cauchy-type integral-based depth-to-basement estimation method to a variety of models to test the reliability of the method in different geological scenarios. I also inverted for three-dimensional (3D) subsurface anomalous density distribution with constrained model parameters in order to produce more compact inversion results. I demonstrated several single-block and multiple-block synthetic model results produced by constrained 3D gravity inversion. I also display results for Cauchy-type integral-based 3D depth-to-basement inversion of simple/complex basin models. The results from both methods are nicely consistent with true models at a very low misfit level and a fast convergence. A case study is presented at the end of our paper for both methods, and results for both methods are used to do interpretation jointly.

In dedication to my mother for making me who I am,

and my fiancé for her support throughout this thesis.

TABLE OF CONTENTS

# ACKNOWLEDGMENTS

I express my heartfelt thanks to my chair, Prof. Michael Zhdanov, for directing this research and always showing me the right course of action during the difficult hours. I also acknowledge support from the University of Utah Consortium for Electromagnetic Modeling and Inversion (CEMI). I am very grateful to USGS for revealing data for public use. I personally thank Dr. Le Wan for his countless help during my research. I am very grateful to Hongzhu Cai for letting me use his algorithm for a part of this thesis. I also thank my advisors at Turkish Oil Corporation (TPAO) for their valuable suggestions on this work, as well as for sharing some of their experience in their different fields of expertise. Finally, I would like to thank all my colleagues for fruitful discussions and constructive criticism throughout this work, and my family for their endless support.

# CHAPTER 1

## INTRODUCTION

Potential field methods have been widely used to identify the physical properties of subsurface formations over decades due to ease of applications and affordability of methods, such as gravity and magnetic methods. The gravity method is one of the most important geophysical methods, which measures a difference of gravity potential on the Earth's surface. Though the gravity method can be used to determine the density variations within the Earth's crust, it is a technique that geophysicists apply to identify the depth, geometry, and density distribution of the anomalous structures, which helps interpreters to understand the geological features of the subsurface (e.g., Mariita, 2007). Furthermore, the gravity method has been effectively used in oil, gas, and geothermal exploration over more than a century.

Generally speaking, the gravity field data are used to determine the anomalous density distribution of the subsurface geological structures. Due to attenuation effect of the gravity data with the distance from the source, and existence of the gravity inverse problem, the inversion results may not be consistent with known geology of the survey area. In some cases, the anomalous bodies may have sharp boundaries that separate them from the surrounding

rocks, such as hydrocarbon (HC) reservoirs or faults. In order to reduce the nonuniqueness, one can use the known geological information and other known physical properties of the rocks to produce a more realistic result. This can be achieved by applying a regularization to the inverse problem solution, which allows us in include the a priori information in the inversion. Over decades, many different approaches to regularized gravity inversion were developed. For example, focusing regularization makes it possible to produce inversion results with sharp boundaries (e.g., Last and Kubik, 1983; Barbosa and Silva, 1994; Portniaguine and Zhdanov, 1999; Zhdanov and Tolstaya, 2004; Zhdanov, 2009). Another approach is based on joint inversion of multiple geophysical data sets to produce a more realistic and unique result by constraining model parameters using the physical/mathematical relationships between different model parameters, for example, density and magnetic susceptibility (e.g., Fedi and Rapolla, 1999; Fan et al., 2008; Shamsipour et al., 2012).

The gravity data are also used for a regional geological/geophysical study. For example, gravity field data can be considered to define the depth to the basement of the Earth's crust. There are many publications considering this problem (e.g., Barbosa et al., 1997,1999a, b; Silva et al., 2001; Williams et al., 2005; Silva et al., 2006, 2007, 2010a, b; Martin et al., 2010, 2011a, b). The conventional approach to providing the depth-to-basement estimate is based on discretization of the sedimental cover into vertical prisms with constant density contrast. In this case, however, the corresponding nonlinear inverse problem becomes computationally very expensive and its solution may require significant

time and computational resources. The Euler deconvolution method introduced by Reid et all. (1990) has been commonly used to estimate the depth to basement using the gravity and magnetic data. However, this method is an approximate one and may lead to erroneous solutions (Cai, 2014).

Zhdanov (2002) demonstrated that the gravity field caused by the sediment-basement interface can be represented as a Cauchy-type surface integral. In the paper by Cai and Zhdanov (2015) it was clearly demonstrated that the Cauchy-type integral representation can be used to estimate the depth of the sediment-basement interface. With this approach, the solution of the problem for depth-to-basement estimation has become computationally less expensive than those using conventional volume integration methods.

In this thesis, I develop and study a constrained reweighted regularized conjugate gradient method (CRRCGM) to produce a more reasonable inversion result than that produced by the conventional methods. I illustrate this new approach by numerical modeling studies. I also apply a depth-to-basement estimation method based on the Cauchy-type integrals to several synthetic models in order to test the reliability of the developed methods in different geological scenarios. Finally, the developed methods are illustrated by a field case study, where both techniques, based on the surface (Cauchy-type) and volume integrals, are used in a framework of a joint interpretation.

# CHAPTER 2

# PHYSICS OF GRAVITY FIELD

## 2.1. Fundamentals of Gravity Field Theory

Here I present a mathematical description of gravity potential and gravity field. First, it is well known that gravity field, g, must satisfy the following equations (Zhdanov, 1988):

$$\nabla \cdot \boldsymbol{g} = -4\pi\gamma\rho, \quad \nabla \times \boldsymbol{g} = 0, \tag{2.1}$$

where $\gamma$ is gravitational constant $(6.672x10^{-11}\ m^3kg^{-1}s^{-2})$ and $\rho$ is anomalous density distribution within domain D.

Generally, gravity field at point $P(x', y', z')$ can be expressed as follows:

$$\boldsymbol{g}(\boldsymbol{r}') = \iiint_V \rho(\boldsymbol{r}) \frac{\boldsymbol{r} - \boldsymbol{r}'}{\left||\boldsymbol{r} - \boldsymbol{r}'|\right|^{\frac{3}{2}}} dv, \tag{2.2}$$

where $r'$ is observation point, defined as; $r' = \sqrt{x'^2 + y'^2 + z'^2}$. The vertical component of the gravity field is:

$$g_z(\boldsymbol{r}') = \iiint_V \rho(r) \frac{z - z'}{\left||\boldsymbol{r} - \boldsymbol{r}'|\right|^{\frac{3}{2}}} dv, \tag{2.3}$$

where $|r - r'| = ((x - x')^2 + (y - y')^2 + (z - z')^2)$ and $dv = dxdydz$.

We can present the expression (2.3) for gravity field at location $(x', y', z')$ in more detail as follows:

$$g_z(x',\ y', z') =$$

$$\gamma \iiint_D \Delta\rho(x, y, z\ ) \frac{z - z'}{((x - x')^2 + (y - y')^2\ + (z - z')^2)^{\frac{3}{2}}}\ dxdydz \tag{2.4}$$

In a short form, the vertical component of gravity field $g_z$ is described by the following formula:

$$g_z(x',\ y', z') = \gamma \iiint_D \Delta\rho(x, y, z\ ) G_z(x - x', y - y', z - z')\ dxdydz, \tag{2.5}$$

where $G_z$ is Green's function for the vertical gravity field, which is defined as follows:

$$G_z(x - x', y - y', z - z') = \frac{z - z'}{((x - x')^2 + (y - y')^2\ + (z - z')^2)^{\frac{3}{2}}}. \tag{2.6}$$

As it is shown in Figure 1, domain *D* is divided into a number of small rectangular cells, where each cell has an anomalous density, $\Delta\rho(x_i,\ y_j,\ z_k)$. In a case of the point mass approximation, the gravity field observed at point $(x',\ y',z')$ can be obtained by a summation of gravity fields caused by every cell, as follows:

$$g_z(x',\ y',z') =$$

$$\sum_{i=1}^{n}\sum_{j=1}^{n}\sum_{k=1}^{n} \Delta\rho(x_i,y_j,z_k)\frac{z-z'}{\left((x_i-x')^2+\left(y_j-y'\right)^2+(z_k-z')^2\right)^{\frac{3}{2}}}\Delta x\Delta y\Delta z \qquad (2.7)$$

where $\Delta x, \Delta y,$ and $\Delta z$ are the size of the cell in the x, y, and z directions, respectively. Thus, a discrete forward modeling operator for gravity field can be expressed in general matrix notation as follows:

$$\mathbf{d} = \mathbf{Am} \qquad (2.8)$$

Here **m** is a vector of model parameters $\left(anomalous\ density\ ,\Delta\rho(x_i,y_j,z_k)\right)$ of the order $N_m$, **d** is a vector of the observed data, $g_z(r')$, of the order $N_d$, and **A** is a rectangular matrix of a size $N_d \times N_m$, formed by the corresponding Green's function values.

## 2.2. Cauchy-type Integral Representation

### 2.2.1. Integral Representation of 2D Gravity Field

It was demonstrated by Zhdanov (2015) that 2D potential field $F$ must satisfy the following equations:

$$\tilde{\nabla} \cdot \boldsymbol{F} = q, \quad \tilde{\nabla} \times \boldsymbol{F} = 0, \tag{2.9}$$

where $\tilde{\nabla}$ and q denote the operator of 2-D differentiation in the vertical plane xz, and the source of potential field $F$, respectively. According to equation (2.9) the scalar components of the vector field satisfy to the following equations inside the source,

$$\frac{\partial F_X}{\partial x} + \frac{\partial F_z}{\partial z} = q(x, z), \tag{2.10}$$

$$\frac{\partial F_X}{\partial z} - \frac{\partial F_z}{\partial x} = 0. \tag{2.11}$$

And outside of the source, respectively,

$$\frac{\partial F_X}{\partial x} + \frac{\partial F_z}{\partial z} = 0,$$

$$\frac{\partial F_X}{\partial z} - \frac{\partial F_z}{\partial x} = 0. \tag{2.12}$$

By introducing complex variable $\zeta = x + iz$, a function $F(\zeta)$ can be defined as follows:

$$F(\zeta) = -F_{x(x,z)} + iF_z(x,z). \tag{2.13}$$

where $F(\zeta)$ is called *a complex intensity of a plane field*. According to equation (2.12), $F(\zeta)$ is an analytical function outside of the source, vanishing at infinity The real and imaginary parts of $F(\zeta)$ satisfy to the Cauchy-Riemann conditions:

$$\frac{\partial ReF}{\partial x} = \frac{\partial ImF}{\partial z},$$

$$\frac{\partial ReF}{\partial z} = -\frac{\partial ImF}{\partial x}. \tag{2.14}$$

Proceeding from the real variables to the complex ones:

$$\zeta = x + iz \quad and \quad \zeta^* = x + iz \tag{2.15}$$

We can introduce the following differential operators:

$$\frac{\partial}{\partial \zeta} = \frac{1}{2}\left(\frac{\partial}{\partial x} - i\frac{\partial}{\partial z}\right), \qquad \frac{\partial}{\partial \zeta^*} = \frac{1}{2}\left(\frac{\partial}{\partial x} + i\frac{\partial}{\partial z}\right), \tag{2.16}$$

where * represents complex conjugate operation. Multiplying equation (2.10) by $(-1)$ and (2.11) by $(-i)$ and summing them up, we obtain;

$$\frac{\partial}{\partial x}(-F_X + iF_z) + i\frac{\partial}{\partial z}(-F_X + iF_z) = -q(x,z), \tag{2.17}$$

$$\frac{\partial}{\partial \zeta^*}F(\zeta) = -\frac{1}{2}q(x,z). \tag{2.18}$$

For an arbitrary function that is analytical in domain S, Cauchy-Riemann relations imply that:

$$\frac{\partial}{\partial \zeta^*}\psi(\zeta) = 0. \tag{2.19}$$

It is shown in Zhdanov (1998) that by using Pompei formula, the solution of the differential equation (2.18) can be obtained as follows:

$$F(\zeta') = \frac{1}{2\pi i}\int_{\partial S}\frac{1}{\zeta - \zeta'}F(\zeta)d\zeta - \frac{1}{\pi}\iint_S \frac{1}{\zeta - \zeta'}\frac{\partial}{\partial \zeta}F(\zeta)ds, \tag{2.20}$$

where $S, \partial S,$ and $\zeta'$ are a domain, boundary, and a fixed point in domain $S$. For any function $\psi$ that is analytical in domain $S$, equation (2.19) is reduced to the well-known Cauchy integral formula:

$$\psi(\zeta') = \frac{1}{2\pi i}\int_{\partial S}\frac{1}{\zeta - \zeta'}\psi(\zeta)d\zeta. \tag{2.21}$$

By applying Pompei formula (2.20) to the system displayed In Figure 2, we obtain the following integral formula:

$$F(\zeta') = \frac{1}{2\pi i}\int_{L_R}\frac{1}{\zeta-\zeta'}F(\zeta)d\zeta + \frac{1}{2\pi}\iint_{S_R}\frac{1}{\zeta-\zeta'}\frac{\partial}{\partial\zeta}q(\zeta)ds, \tag{2.22}$$

After integration over $L_R$ and substitution of variables, $\zeta = \zeta' + R\cdot e^{\theta i}$, we have:

$$\frac{1}{2\pi i}\int_{L_R}\frac{1}{\zeta-\zeta'}F(\zeta)d\zeta = \frac{1}{2\pi}\int_{-\pi}^{\pi}F\left(\zeta' + R\cdot e^{\theta i}\right)d\theta. \tag{2.23}$$

As $R\to\infty$, limit of the equation (2.23) is zero. Thus, we finally arrive at the following equation:

$$F(\zeta') = \frac{1}{2\pi}\iint_{\Gamma}\frac{1}{\zeta-\zeta'}q(\zeta)ds, \tag{2.24}$$

where $q(\zeta) = 0\ if\ \zeta \notin \Gamma$.

The gravity field $g$ of a two-dimensional mass having a density $\rho(x,z)$ within the domain $\Gamma$ satisfies equation (2.1) (Zhdanov, 1998 and 2015).

Complex intensity of the gravity field is defined as follows:

$$g(\zeta) = -g_x(x,z) + ig_z(x,z) \tag{2.25}$$

According to equation (2.18, function ) $g(\zeta)$ satisfies to the following equation:

$$(\partial/\partial\zeta^*)\ g(\zeta) = 2\pi\gamma\rho, \tag{2.26}$$

where its solution is as follows:

$$g(\zeta) = -2\gamma \iint_{\Gamma} \frac{1}{\zeta - \zeta'} \rho(\zeta) ds, \tag{2.27}$$

where $\gamma$ is gravitational constant, and $\rho(\zeta)$ is density of the source located at point $(x, z)$.

2.2.2. Three-Dimensional Cauchy-type Integral

In this part, I briefly discuss an application of the 3D Cauchy-type integrals to the solution of the inverse problem for the depth-to-basement estimation (Cai, 2014). It was first introduced by Zhdanov (2002) that gravity field caused by a sediment-basin interface can be represented using 3D Cauchy-type integrals. This approach makes it possible to reduce a three-dimensional (3D) inverse problem to a two-dimensional (2D) one, where the inverse problem is solved only for the depth of the sediment-basement interface.

The gravity field caused by a 3D body D with a constant density can be represented as follows (Zhdanov, 1988; Zhdanov and Lui, 2013):

$$\boldsymbol{g}(\boldsymbol{r}') = \frac{4\pi G \rho_0}{3} [\boldsymbol{C^s}(\boldsymbol{r}' - \boldsymbol{r}) - \boldsymbol{C^s}(\boldsymbol{r}' - \boldsymbol{r}')] = \frac{4\pi}{3} G \rho_0 \boldsymbol{C}^s(\boldsymbol{r}', \boldsymbol{r} - \boldsymbol{r}'), \tag{2.28}$$

where $\boldsymbol{C}^s$ is a Cauchy-type integral introduced by Zhdanov (1988) as follows:

$$\boldsymbol{C^s}(\boldsymbol{r}', \boldsymbol{\varphi}) = -\frac{1}{4\pi} \iint_s \left[ (\boldsymbol{n} \times \boldsymbol{\varphi}) \nabla \frac{1}{|r - r'|} + (\boldsymbol{n} \times \boldsymbol{\varphi}) \times \nabla \frac{1}{|r - r'|} \right] ds. \tag{2.29}$$

Equation (2.28) can be written using matrix notations as follows:

$$g_\alpha = -\frac{G\rho_0}{3}\iint_s \Delta_{\alpha\beta\gamma\eta}\frac{(r_\beta - r'_\beta)(r_\eta - r'_\eta)}{|\boldsymbol{r}-\boldsymbol{r}'|}ds \tag{2.30}$$

where $\alpha, \beta, \gamma, \eta = x,\ y,\ z$, and Δ-symbol is expressed as follows:

$$\Delta_{\alpha\beta\gamma\eta} = \delta_{\alpha\beta}\delta_{\gamma\eta} + \delta_{\alpha\eta}\delta_{\beta\gamma} - \delta_{\alpha\gamma}\delta_{\beta\eta}; \delta_{\alpha\beta} == \begin{cases} 1, & \alpha = \beta \\ 0, & \alpha \neq \beta \end{cases} \tag{2.31}$$

## 2.3. 3D Gravity Field Based on 3D Cauchy-type Representation

In a case of the conventional depth-to-basement estimation, the model domain is divided into vertical prisms, and total gravity field is calculated as a summation of gravity fields caused by each prism column (see Figure 3). Each vertical prism has $dx$ and $dy$ size in the x and y directions, respectively. Each prism has a constant density contrast value. Thus, the inversion is applied in order to estimate the thickness of each prism in the z-direction, which is equal to $|z_1 - z_2|$. Obviously, this inverse problem is ill-posed, and it may require using significant computational resources in order to complete this inversion due to integration over a 3D volume filled with the sediments.

In 1988, a new method of the solution of geophysical forward and inverse problems using Cauchy-type integrals was introduced by M.S. Zhdanov. This method made it possible to reduce a 3D geophysical problem to the 2D one. This method helps to reduce the computational demand and to decrease the time

consumption. It also makes the problem easier to understand. Generally, the method assumes that gravity field on the surface above a valley or a basin is caused by a sediment-basement interface, which may have a constant or functionally decreasing (with depth) density contrast. Similar to the conventional method, the sediment-basement interface is divided into some cells in the x and y directions. Figure 4 shows that, now the problem is reduced to 2D integration of the surface of the interface. However, the solution of this inverse problem is still ill posed.

It was presented by Cai (2014, 2015) that gravity field caused by a sediment-basement interface can be represented by Cauchy-type integrals. Let's consider a model of a sediment-basement interface, where the density is constant and does not vary with depth. The surface of the sediment-basement interface can be described by equation $z = h(x, y) - H_0$, where $H_0$ is a horizontal reference. The gravity field caused by the sediment deposit is calculated as follows (Zhdanov, 1988):

$$\boldsymbol{g}(\boldsymbol{r}') = 4\pi G\rho_0 \boldsymbol{C}^s(\boldsymbol{r}', (z - H_0)\boldsymbol{dz}), \tag{2.32}$$

where $\rho_0$ is a density contrast of the sediment-basement interface. It is defined by the following formula:

$$\rho_0 = \rho_b - \rho_s > 0 \tag{2.32}$$

where $\rho_b$ is basement density, $\rho_s$ is sediment density. Equation (2.9) is described in matrix notation as follows:

$$\boldsymbol{g}_{\alpha}(\boldsymbol{r}') = -G\rho_0 \iint_s \Delta_{\alpha\beta\gamma\eta} \frac{h(x,y)(r_\eta - r_\eta{}')}{|\boldsymbol{r} - \boldsymbol{r}'|}\, b_\gamma dxdy, \tag{2.34}$$

where $b_\gamma$ is a function defined as follows:

$$b_x(x,y) = \frac{\partial h(x,y)}{\partial x}, b_y(x,y) = \frac{\partial h(x,y)}{\partial y}, and\ b_z(x,y) = 1. \tag{2.35}$$

Thus, the discrete forward modeling operator for the gravity field can be expressed in general matrix notations as follows:

$$\boldsymbol{d} = \boldsymbol{A}^C \boldsymbol{m} \tag{2.36}$$

Here **m** is a vector of model parameters $\left(depth - to - basement, h(x_i, y_j)\right)$ of the order $N_m$, **d** is a vector of the observed data, $g_z(r')$, of the order $N_d$, and $\boldsymbol{A}^C$ is a rectangular matrix of a size $N_d \times N_m$, formed by the corresponding Cauchy-type gravity field kernels.

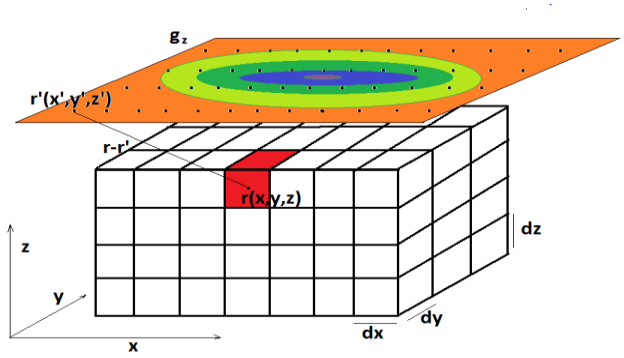


Figure 1: Discretization of domain D using rectangular cells.

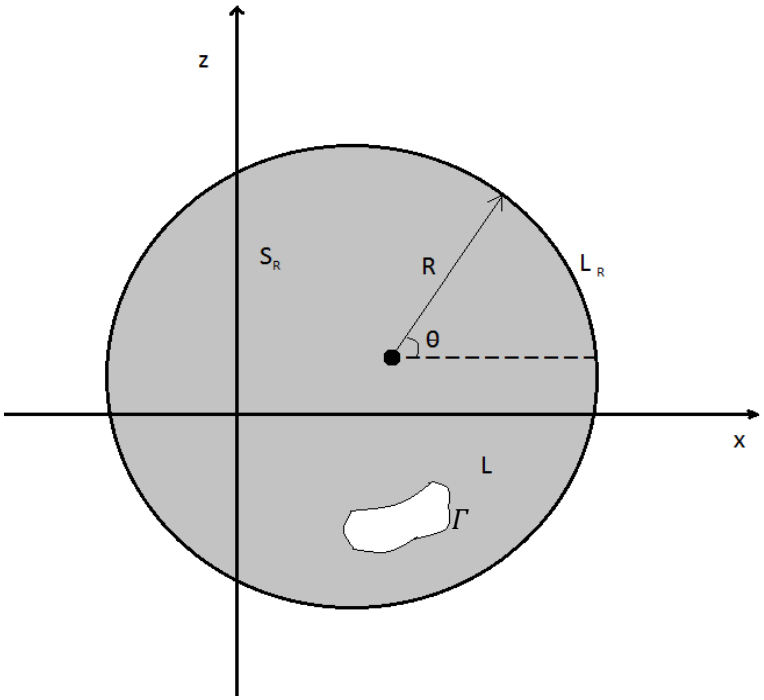


Figure 2: A plot illustrating a solution of the equation for the complex intensity of the potential field using the Pompei formula. $\Gamma$ is the domain occupied by the field source (after Zhdanov, 2015).

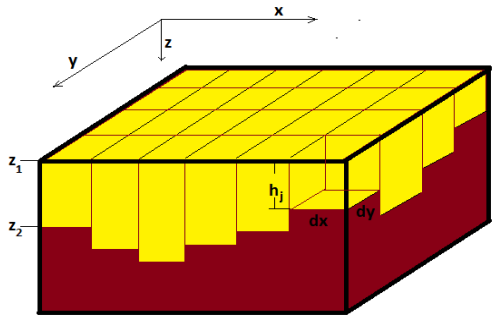


Figure 3: Model discretization for conventional forward and inverse modelling.

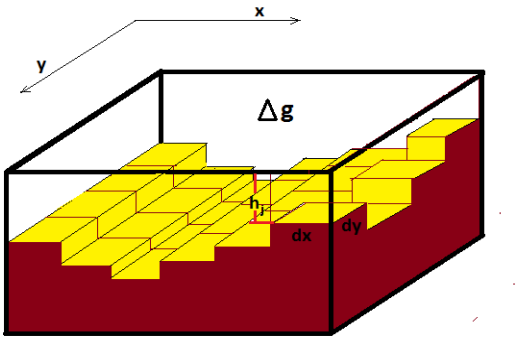


Figure 4: Discretization of the sediment-basement interface for forward and inverse modelling using Cauchy-type integrals.

# CHAPTER 3

# PRINCIPLES OF REGULIZED INVERSION OF GRAVITY DATA

## 3.1. Inversion of Gravity Data Based on the Volume Integral Method

In a general case, there are two major geophysical problems, forward modeling and inversion problems. The forward modeling can be expressed by computing a map of geophysical data based on some known information of the physical properties of the subsurface. However, in the inverse problem solution, one is required to find a model of subsurface physical properties that fits the data. A solution of the inverse problem has been used in almost all geophysical prospecting methods such as gravity, magnetic, seismic, and electromagnetic (EM) methods to find the geologically and mathematically meaningful causative structures within the Earth's crust.

Similar to other methods, it is well known that the gravity inverse problem is an ill-posed problem due to instability and nonuniquenes of the inversion solution (Zhdanov, 2002). For example, a gravity field observed on the surface of the Earth can be computer simulated using a number of the density models beneath the Earth's surface. That is, the gravity inverse problem is nonunique. It was thought that there was no a solution to such a problem until the time of the famous Russian mathematician Tikhonov (Zhdanov, 2002). After his theory

(regularization method), even an ill-posed inverse problem can be made a well-posed problem.

In addition to the theoretical part of the inversion method, in order to have an efficient result, the interpreter should apply geological properties of the expected causative mass/masses, and also consider the geometrical features of the main target. After inversion, it is inevitable to see a density concentration close to the surface due to the fact that gravity is inversely proportional to the depth. Since gravity field and resolution decrease with the depth of the target, during the inversion process, the model weighting must be applied in order to produce a correct result.

In summary, we can schematically describe the forward and inverse problems as shown below.

Forward modeling problem;

$$\text{model (m)} \rightarrow \text{data (d)}$$

Inverse problem;

$$\text{data (d)} \rightarrow \text{model (m)}$$

In equation (2.36), the gravity inversion is reduced to the solution of a linear matrix equation. This inverse problem is ill posed, i.e., the solution can be nonunique and unstable. To solve such a problem, one needs to use the regularization theory (Tikhonov and Arsenin, 1977; Zhdanov, 2002). In conventional way, one substitutes the solution of the linear inverse problem (2.8) with the minimization of the Tikhonov parametric functional:

$$P^{\alpha} = \phi(\boldsymbol{m}) + \alpha \boldsymbol{s}(\boldsymbol{m}) = min, \tag{3.1}$$

where the misfit functional, $\phi(\boldsymbol{m})$, is specified as:

$$\phi(\boldsymbol{m}) = \left|\left|\boldsymbol{W_d}(\boldsymbol{Am} - \boldsymbol{d})\right|\right|^2. \tag{3.2}$$

The stabilizer is selected to be minimum norm functional:

$$s(\boldsymbol{m}) = \left|\left|\boldsymbol{W_m}\left(\boldsymbol{m} - \boldsymbol{m_{apr}}\right)\right|\right|^2, \tag{3.3}$$

where $\boldsymbol{W_m}$ and $\boldsymbol{W_d}$ are model weighting and data weighting matrices, respectively. The minimization problem (3.1) can be solved using the regularized conjugate gradient (RCG) method (Zhdanov, 2002).

3.1.1. Regularized Conjugate Gradient Method (RCGM)

The minimization problem (2.9) can be solved using the regularized conjugate gradient method. The RCG method is formed by the following iterative process (Zhdanov, 2002).

$$\boldsymbol{m_{n+1}} = \boldsymbol{m_n} + \boldsymbol{\delta m} = \boldsymbol{m_n} - \boldsymbol{k_n^{\alpha}}\tilde{\boldsymbol{I}}^{\alpha}(\boldsymbol{m_n}). \tag{3.4}$$

The conjugate gradient directions $\tilde{\boldsymbol{I}}^{\boldsymbol{\alpha}}(\hat{\boldsymbol{m}}_{\boldsymbol{n}})$ are selected as follows. In the initial step, one uses the “direction” of regularized steepest ascent for the initial model:

$$\tilde{\boldsymbol{I}}(\boldsymbol{m_0}) = \boldsymbol{I}^{\alpha}(\boldsymbol{m_n}) = \boldsymbol{F_{m_0}}\boldsymbol{W_d^2}(\boldsymbol{A}(\boldsymbol{m_0}) - \boldsymbol{d}) + \alpha\boldsymbol{W_m^2}\left(\boldsymbol{m_0} - \boldsymbol{m_{apr}}\right), \tag{3.5}$$

where Frechet derivative matrix, $\boldsymbol{F_{m_0}}$, is defined by the following formula:

$$\boldsymbol{F_{m_0}} = \frac{\boldsymbol{\partial A(m_0)}}{\boldsymbol{\partial m}}. \tag{3.6}$$

In the next step, the "direction" of ascent is defined as a linear combination of the regularized steepest ascent in this step and the "direction" of ascent $\tilde{\boldsymbol{I}}(\boldsymbol{m_0})$ in the previous step:

$$\tilde{\boldsymbol{I}}^{\alpha}(\boldsymbol{m_1}) = \boldsymbol{I}^{\boldsymbol{\alpha}}(\boldsymbol{m_1}) + \beta_1^{\alpha}\tilde{\boldsymbol{I}}^{\alpha}(\boldsymbol{m_0}). \tag{3.7}$$

In the $(n+1)$ step:

$$\tilde{\boldsymbol{I}}^{\alpha}(\boldsymbol{m_n}) = \boldsymbol{I}^{\boldsymbol{\alpha}}(\boldsymbol{m_{n+1}}) + \beta_{n+1}^{\alpha}\tilde{\boldsymbol{I}}^{\alpha}(\boldsymbol{m_n}), \tag{3.8}$$

where the regularized steepest ascent directions are determined now according to the formula:

$$\boldsymbol{I}^{\alpha}(\boldsymbol{m_n}) = \boldsymbol{F_{m_n}}\boldsymbol{W_d^2}(\boldsymbol{A}(\boldsymbol{m_n}) - \boldsymbol{d}) + \alpha\boldsymbol{W_m^2}(\boldsymbol{m_n} - \boldsymbol{m_{apr}}). \tag{3.9}$$

For iteration $n$, Frechet derivative is determined by the formula:

$$\boldsymbol{F_{m_n}} = \frac{\boldsymbol{\partial A(m_n)}}{\boldsymbol{\partial m}}. \tag{3.10}$$

The step length of each iteration, the coefficient $k_n^{\alpha}$, can be determined with a linear line search:

$$k_n^{\alpha} = \frac{\left(\boldsymbol{I}^{\alpha}(\boldsymbol{m_n}), \tilde{\boldsymbol{I}}^{\alpha}(\boldsymbol{m_n})\right)}{\left(\tilde{\boldsymbol{I}}^{\alpha}(\boldsymbol{m_n}), \boldsymbol{F}_{\boldsymbol{m_n}}^{\boldsymbol{T}}\boldsymbol{F}_{\boldsymbol{m_n}}\tilde{\boldsymbol{I}}^{\alpha}(\boldsymbol{m_n}) + \boldsymbol{\alpha_n}\tilde{\boldsymbol{I}}^{\alpha}(\boldsymbol{m_n})\right)}. \tag{3.11}$$

One can use a parabolic line search also (Zhdanov, 2002) to improve the convergence rate of the RCG method. The conjugate gradient (CG) method requires that vectors $\tilde{\boldsymbol{I}}^{\alpha}(\boldsymbol{m_n})$, introduced above, will be mutually conjugated. This requirement is fulfilled if the coefficients $\beta_n$ are determined by the formula:

$$\beta^{\alpha}{}_{n+1} = \frac{\left|\left|\boldsymbol{I}^{\alpha}(\boldsymbol{m_{n+1}})\right|\right|^2}{\left|\left|\boldsymbol{I}^{\alpha}(\boldsymbol{m_n})\right|\right|^2}. \tag{3.12}$$

Using equations (3.1) to (3.12), one can obtain $\boldsymbol{m}$ iteratively. It is called *regularized conjugate gradient optimization* (Zhdanov, 2002).

Here I present two different ways to decrease the regularization parameter, $\alpha$, adaptively for the depth-to-basement estimation and three-dimensional anomalous density distribution, respectively.

The regularization parameter for the depth-to-basement estimation can be calculated as follows:

$$\alpha_1 = \left|\left|\phi(\boldsymbol{m}_1)\right|\right|^2 / \left|\left|s(\boldsymbol{m}_1)\right|\right|^2, \tag{3.13}$$

where initial regularization parameter $\alpha_0 = 0$. For iteration $n$:

$$\alpha_n = q_c \alpha_{n-1}\,, \quad 0 < q_c < 1 \tag{3.14}$$

If there is an increase in the stabilizer, the following condition will be considered:

$$\alpha_n = \begin{cases} \alpha_{n-1}, & \gamma \le 1 \\ \dfrac{\alpha_{n-1}}{\gamma}, & \gamma > 1 \end{cases}, \tag{3.15}$$

where variable $\gamma$ is defined by the formula:

$$\gamma = \frac{\left(\boldsymbol{s}(\boldsymbol{m}_n)\right)}{(\boldsymbol{s}(\boldsymbol{m}_{n-1}))}. \tag{3.16}$$

The regularization parameter for the anomalous density distribution can be determined as follows:

$$\alpha_1 = \frac{\left|\left|\boldsymbol{\phi}(\boldsymbol{m_1})\right|\right|^2}{\left|\left|\boldsymbol{s}(\boldsymbol{m_1})\right|\right|^2}, \tag{3.17}$$

where initial regularization parameter $\alpha_0 = 0$. For iteration $n$:

$$\alpha_n = q_c^{n-1} \alpha_1\,. \tag{3.18}$$

The algorithm of the RCG method can be summarized as follows:

- $\boldsymbol{r_n = W_d(A(m_n) - d_{obs})}$ ,
- $\boldsymbol{W_m = diag\left(F'_{m_n} * F_{m_n}\right)^{\frac{1}{4}}}$,
- $\boldsymbol{l_n^{\alpha_n} = l^{\alpha_n}(m_n) = F^*_{m_n} r_n + W_m * \alpha * \left(m_n - m_{apr}\right)}$,
- $\boldsymbol{\beta_n^{\alpha} = \left|\left|l_n^{\alpha}\right|\right|^2 / ||l_{n-1}^{\alpha}||^2}$,
- $\boldsymbol{\check{\mathrm{I}}_n^{\alpha} = l_n^{\alpha} + \beta_n^{\alpha} \check{\mathrm{I}}_{n-1}^{\alpha}}$ , $\boldsymbol{\check{\mathrm{I}}_0^{\alpha} = l_0^{\alpha}}$,
- $\check{\mathrm{k}}_n^{\alpha} = \frac{(\check{\mathrm{I}}_n^{\alpha},\, l_n^{\alpha})}{,\left(norm\left(F_{m_n} \check{\mathrm{I}}_n^{\alpha}\right)^2 + \alpha * norm\left(W_m \check{\mathrm{I}}_n^{\alpha}\right)\right)}$,
- $\boldsymbol{m_{n+1} = m_n + \Delta m}$ , $\quad \boldsymbol{\Delta m = -\check{\mathrm{k}}_n^{\alpha} \check{\mathrm{I}}_n^{\alpha}}$ .

The regularization parameter for the depth-to-basement inversion is given by the following formula:

- $\alpha_1 = \frac{||W_d A(m_n) - W_d d_{obs}||^2}{||W_m m_n - W_m m_{apr}||^2}$,, $\quad \alpha_{n-1} = \alpha_1 * (q_c)^{iter-2}$, $\quad \alpha_0 = 0$
- $\alpha_n = \begin{cases} \alpha_{n-1}, \ \gamma \leq 1 \\ \frac{\alpha_{n-1}}{\gamma}, \ \gamma > 1 \end{cases}$

The regularization parameter for the density contrast inversion is defined as shown below:

$$\alpha_1 = ||\boldsymbol{A}(\boldsymbol{m_n}) - \boldsymbol{d_{obs}}||^2/||\boldsymbol{m_n} - \boldsymbol{m_{apr}}||^2\,, \quad \alpha_{n-1} = \alpha_1 * (q_c)^{iter-2}, \quad \alpha_0 = 0$$

3.1.2. Constrained and Reweighted Regularized Conjugate Gradient Method

Due to nonuniqueness of the gravity inverse problem, the inversion results may contain some artificial numbers, which are not consistent with the true model. Also, the inversion process can produce results with poor depth resolution. To overcome these difficulties, I have applied Minimum Support (MS) stabilizer and solved the problem in logarithmic space to constrain the inversion in order to produce more compact and reasonable results.

During surveys, it is possible to have a priori estimation that the model parameters exist within some intervals (Zhdanov, 2015):

$$m_i^- \le m_i \le m_i^+, \quad i = 1,2,3, \dots L, \tag{3.19}$$

where $m_i^-$ and $m_i^+$ are lower and upper boundaries of the model parameters. However, in a general case, the inversion process may produce the model parameters outside of these intervals. By transforming the model parameters, $\boldsymbol{m}$, into a space of parameters, $\widetilde{\boldsymbol{m}}$, so that the scalar components of original $\boldsymbol{m}$ always remain within the interval, we can enforce the above constrains in the solutions. A conventional way to solve this problem is to apply a logarithmic space of model parameters by introducing:

$$m_i = \ln((m_i - m_i^-)/(m_i^+ - m_i)) \;\; = \ln(m_i - m_i^-) - \ln(m_i^+ - m_i). \tag{3.20}$$

in matrix notations:

$$\tilde{\boldsymbol{m}} = \ln(\boldsymbol{m} - \boldsymbol{m}^{-}) - \ln(\boldsymbol{m}^{+} - \boldsymbol{m}), \tag{3.21}$$

where $\boldsymbol{m}^{-}$ and $\boldsymbol{m}^{+}$ are column vectors having the same length.

Inverse transform of the model parameters in matrix notation is:

$$\boldsymbol{m} = \left(\hat{\mathbf{I}} + \exp\left(\widehat{\tilde{\boldsymbol{m}}}\right)\right)^{-1}\left(\boldsymbol{m}^{-} + exp\left(\widehat{\tilde{\boldsymbol{m}}}\right)\boldsymbol{m}^{+}\right), \tag{3.22}$$

where $\widehat{\tilde{\boldsymbol{m}}}$ is a diagonal matrix of parameters. In this case, Frechet matrix will also change in a following form:

$$F = \Delta m \mathbf{A}\left[\hat{\mathbf{I}} + \exp(\tilde{\boldsymbol{m}})\right]^{-2}[\exp(\tilde{\boldsymbol{m}})]. \tag{3.23}$$

In order to produce a focused inversion result with sharp boundaries at the edges, I have used a focusing minimum support stabilizer (Zhdanov, 2002, 2015).

To update the minimum support functional, I used weighting matrix, $\widetilde{W}_e$:

$$\widetilde{\boldsymbol{W}}_e = diag\left[(\tilde{\boldsymbol{m}}^2 + e^2)^{\frac{1}{2}}\right] \approx diag[|\tilde{\boldsymbol{m}}|], if\ e \to 0 \tag{3.24}$$

## 3.2. Inversion of Gravity Data Based on Cauchy-type Integral Representation

In this thesis, I have developed an algorithm and conducted inversion of gravity data, $g_z$, using 3D Cauchy-type integral representation. The analytical solution for the vertical component of the gravity field is shown in equation (2.30). It is presented in a simpler way by Cai and Zhdanov (2015) as follows:

$$g_z(\boldsymbol{r}_n{}') = \sum_{k=1}^{N_m} f_z^{(nk)} h^{(k)}, \tag{3.25}$$

$$f_z^{(nk)} = -G\gamma\rho_0 \frac{z^{(k)} - z^{(n)}{}'}{|\boldsymbol{r}^{(k)} - \boldsymbol{r}_n'|^3} \Delta x \Delta y = -G\gamma\rho_0 \frac{h^{(k)} - H_0 - z^{(n)}{}'}{|\boldsymbol{r}^{(k)} - \boldsymbol{r}_n'|^3} \Delta x \Delta y. \tag{3.26}$$

By taking a derivative of equation (3.25) with respect to h, one can find the solution for the Frechet matrix. It is shown as follows:

$$F_{nl} = \frac{\partial g_z(\boldsymbol{r}_n')}{\partial h^{(l)}} = \frac{\partial \sum_{k=1}^{N_m} f_z^{(nk)} h^{(k)}}{\partial h^{(l)}} \tag{3.27}$$

$$= \partial \sum_{k=1}^{N_m} \left[ \frac{\partial f_z^{(nk)}}{\partial h^{(l)}} h^{(k)} + \frac{\partial h^{(k)}}{\partial h^{(l)}} f_z^{(nk)} \right],$$

where

$$\frac{\partial h^{(k)}}{\partial h^{(l)}} = \delta_{kl}. \tag{3.28}$$

$$\frac{\partial f_z^{(nk)}}{\partial h^{(l)}} = -G\gamma\rho_0\Delta x\Delta y \frac{\partial}{\partial h^{(l)}}\left[\frac{h^{(k)} - H_0 - z^{(n)'}}{|\boldsymbol{r}^{(k)} - \boldsymbol{r}_n'|^3}\right] \tag{3.29}$$

$$= G\gamma\rho_0\Delta x\Delta y\left[3\frac{\left(h^{(k)} - H_0 - z^{(n)'}\right)^2}{|\boldsymbol{r}^{(k)} - \boldsymbol{r}_n'|^5} - \frac{1}{|\boldsymbol{r}^{(k)} - \boldsymbol{r}_n'|^3}\right].$$

By substituting equation (3.29) into (3.27), one can arrive at the following expression for the Frechet derivative:

$$F_{nl} = \frac{G\gamma\rho_0\Delta x\Delta y}{|r^{(l)} - r_n'|^3}\left[\frac{3\left(h^{(k)} - H_0 - z^{(n)'}\right)^2}{|\boldsymbol{r}^{(k)} - \boldsymbol{r}_n'|^2}h^{(l)}\right. \tag{3.30}$$

$$\left. - \left(2h^{(l)} - H_0 - z^{(n)'}\right)\right]$$

One can find the components of the Frechet derivative matrix as it is shown below:

$$F_{\alpha v}^{(nl)} = \frac{G\gamma\rho_0\Delta x\Delta y h^{(l)}}{|\boldsymbol{r}^{(l)} - \boldsymbol{r}_n'|^5}[3\delta_{zv}\left(r_\alpha^{(l)} - r_\alpha^{(n)'}\right) + 3\delta_{z\alpha}\left(r_v^{(l)} - r_v^{(n)'}\right)$$

$$+2\delta_{v\alpha}\left(h^{(l)} - H_0 - z^{(n)'}\right)]$$

$$+\frac{G\gamma\rho_0\Delta x\Delta y p_{\alpha v}^{(nl)}}{|\boldsymbol{r}^{(l)} - \boldsymbol{r}_n'|^5}\left(1 - 5h^{(l)}\frac{h^{(l)} - H_0 - z^{(n)'}}{|\boldsymbol{r}^{(l)} - \boldsymbol{r}_n'|^2}\right) \tag{3.31}$$

# CHAPTER 4

# NUMERICAL STUDIES

## 4.1. Depth-to-Basement Estimation

I have tested the developed method of the depth-to-basement estimation based on the Cauchy-type integral using several different synthetic models. For all models, I considered the same size of the modeling domain, the cell size, the density contrast, and the depth to the top boundary of the basin, $H_0$. The results mostly correspond well to the true model. I used the Bouguer slab formula to calculate an initial model for the inversion in order to start with the lower misfit at the first iteration. It is defined by the following formula:

$$h_{initial}(x, y) = 2\pi G \Delta\rho g_z(r') \tag{4.1}$$

where $G$ is gravitational constant ($6.672x10^{-11}m^3kg^{-1}s^{-2}$), $\Delta\rho$ is density contrast, and $h(x, y)$ is thickness of slab at different locations. Based on the inversion results for synthetic models, the behavior of inversion was analyzed in order to select the optimal workflow for the real data study.

### 4.1.1. Model 1: A Simple Basin Model

#### 4.1.1.1. *Description of Model 1*

Model 1 is shown in Figure 5. The deepest part of the basin reaches down to 490 m, and shallowest part gets close to 0. The density contrast is chosen to be $0.4\ \mathrm{gr/cm^3}$, and the cell size is 100 m*100 m in the x and y directions, respectively. The observations were made 30 m above the ground at the point with the spacing of 100 m in the x and y directions. The forward modeling was done based on the Cauchy-type integral representation. A noise-free vertical component of the gravity field ($G_z$ in mGal) is shown in Figure 6.

#### 4.1.1.2. *Inversion Result*

The inversion domain was divided into the same number and size of cells that were used to compute the gravity data. The inversion was run on a personal computer (Intel Core i5, 4G RAM, 2.67GHz). The tolerance for inversion was fixed to be 0.5%. The misfit reached this level at the 7$^{th}$ iteration. The relative misfit value versus iteration number is plotted in Figure 7. Applying Bouguer slab formula (4.1) to create an initial model based on the observed data set helps inversion to begin with a relative misfit as low as 20% for the 1$^{st}$ iteration.

A 3D inversion result is shown in Figure 8. There is also a plot of cross section over the center of the true model and of the inversion result. The inversion result fits very well to the true model as is seen in Figure 9. The inversion was able to recover the shallower parts of the model very well; however, the deepest part and edges of the model are not recovered well

enough due to decrease to sensitivity of potential data with depth. At the edges, we observe a typical effect of ambiguity of the inversion result because the inversion assigns zero “0” values to the area outside of the observation domain, which forces the inversion to fit the data by adding additional masses at the edges. For the deepest part, by fixing the maximum thickness of the sediment deposit, we can produce a better result and the sharper boundaries.

#### 4.1.2. Model 2: A Complex Basin Model

In a real situation, the basin may have a more complex geology than one considered above. In order to address this issue, I have built Model 2 with multiple deeps to estimate the depth-to-basement relief.

##### 4.1.2.1. *Description of Model 2*

Model 2 has two major deeps that have the same orientation in the y axis but different in the x axis. The eastern part of the basin model is deeper than the western part; however, they have the same surface area in the x-y plane view. This would help us to see how the method will treat a deeper part of the basin where the extensional zones may occur (Bottrill et al., 2012).

Figure 10 shows a true complex basin model. The deeper part of the basin model reaches down to 300 m, and the lowest part get close to the surface upward. A sediment deposition is set to have a density contrast of $0.4\ \mathrm{g/cm^3}$ . The top of the basin reaches up to the surface of the Earth.

A noise-free vertical gravity field for Model 2 was computed using the Cauchy-type integral, and the result was plotted in Figure 11. The observation

points were located at 30 m above the surface of the Earth with 100 m spacing in the x and y directions. As it is expected, the deeper part has the lowest $G_z$ value since it has the thickest sediment deposition.

4.1.2.2. *Inversion Result*

Iterative inversion of the gravity data for the complex basin Model 2 took eight iterations to reach the relative misfit level of 1% (see Figure 12). The first iteration started with a misfit of ~17 % thanks to a proper initial model created by Bouguer slab formula (4.1).

Since the top of the basin is located at the surface of the Earth, the inversion produces sharp edges in order to fit the data with the given initial parameters (see Figure 13). A plot of cross sections along the y axis is displayed in Figure 14. According to this plot, one can see that the shallower part of the model is fitted better than the deep one. As it was mentioned above, this is caused by a decrease of the sensitivity of the gravity field data with depth.

4.1.3. Model 3: Complex Basin Model with Poor Data Coverage

I have formed a new model, which does not have good data coverage for the deepest part of the basin. This Model 3 should show how the depth-to-basement estimation method based on the Cauchy-type integral performs in the situation typical for the field measurements, where the observation points may not cover the major anomalous areas due to geographical and/or logistic problems.

4.1.3.1. *Description of Model 3*

A 3D view of basin Model 3 is shown in Figure 15. The basin has an unclosed contour of the surface on the east side, where the basin has the deepest part. The density contrast of sediment deposit is of $0.4\ \mathrm{g/cm^3}$. The deepest part of the basin goes down to 250 m in the z direction. The shallower part of the basin reaches the Earth's surface. The synthetic observed data computed using the Cauchy-type integral is displayed in Figure 16. In the numerical experiment, I have only considered a part of the data within a rectangle area shown in Figure 17.

4.1.3.2. *Inversion Result*

I ran the information for the data point located within the white rectangle shown in Figure 17. For this particular synthetic study, the relative misfit was set to 0.035 for termination of the iterative inversion (see Figure 18). The inversion results are shown in Figures 19 and Figure 20. One can see that the depth to the basement was well recovered where the data coverage is good; however, the inversion did not produce a good result for the part of the basin where data coverage is poor. In such scenarios, a plot of absolute differences between the observed and predicted data may help the interpreter to define a reliable target area for further interpretation.

## 4.2. Volume Density Inversion

In this section, I will present the results of conventional volume density inversion using reweighted regularized conjugate gradient (CRRCG) method.

### 4.2.1. A single-block Model

#### 4.2.1.1. *Description of Model 4*

For a single-block model, a block is located at different depths and has different sizes (see Figure 21 and 22). The block is divided into rectangular cells with constant anomalous density. Figure 23 presents the synthetic observed vertical gravity field data. The observation points are located above ground at 30 m and observation spacing in x and y direction is 100 m evenly.

#### 4.2.1.2. *Inversion Result*

I have tested the developed inversion algorithms based on CRRCG and RCG methods. Results are shown at the end of the chapter.

4.2.1.2.1. Inversion without constraints and focusing. Figures 24 and 25 show the inversion results for Model 4. The iterative inversion was terminated at the 33th iteration when the misfit reached 1 %. Figure 25 presents the Horizontal (top panel) and vertical (bottom panel) cross sections of the inversion results. However, the inverse model is dispersed at the bottom of the domain due to decrease of the sensitivity of the gravity field with the depth.

4.2.1.2.2. Inversion with constraints and focusing. In the second set of numerical experiments for the Model 4, we set the density constraints, boundaries of the logarithmic space transformation, to be symmetric, e.g.,

$1g/cm^3 \leq m_i \leq 1g/cm^3$. Figure 26 presents the plots of the relative misfit, parametric functional, and stabilizer versus the iteration number, observed gravity field, and predicted gravity field data for constrained and focused inversion. The results of the constrained and focusing (reweighted) inversion shown in Figure 27 demonstrate that the algorithm is capable of recovering the true model location and the anomalous density distribution well.

I have also tested the CRRCG and RCG methods for shallower block Model 5 and 6 to compare the results with true model properties. The inversion used the same parameters (inversion domain, cell size, and observation spacing) as for Model 4. In Figure 28, I demonstrated results for single-body buried model studies. For single-body study with CRRCG method, as the anomalous block gets closer to the surface, it takes more iterations to reach termination criteria; however, inversion produces results closer to the true model, and the location of the anomalous body gets easier to identify (Figure 28, top-right and bottom-right). In Figure 28, inversion results with RCG method are shown on the left; results with CRRCG method are on the right side. One can see that with constrained inversion, it is more efficient to locate a shallower and deeper body that is denser around the center.

I have also tested constrained and focused inversion with a non-zeros background model (Model 7). The location of the anomalous body is shown in Figure 29. The depths to the top and bottom of the block are 100 m and 1100 m, respectively, and it has a density of 1 $\mathrm{g/cm^3}$. The homogeneous background half space has a density of 0.4 $\mathrm{g/cm^3}$.

Inversion domain has a size of 5700 m x 5700 m x 2700 m in x, y, and z directions, respectively. Cell size for inversion is set to be 100 m x 100 m x 100 m. Inversion result is shown in Figure 30. Inversion results demonstrate that the constrained and focused inversion algorithm is capable of recovering the depth of the true model with concentrated model parameters at the center of the anomalous body (see Figure 30, bottom-left).

I have also tested the constrained and focused inversion approach for Model 8 with a basement-like structure (see Figure 31). Inversion result is demonstrated in Figure 32. From the results (see Figure 32), it is clear that constrained and focused inversion produced 3D density distribution where the anomalous body location is matched with the true model location. Also, inversion was capable of recovering a basement-like part that is consistent with the true model location.

### 4.2.2. A Two-block Model

In this part, I have inverted the gravity data for Model 9 consisting of two blocks placed at different depths, where both bodies have the same size and anomalous density.

#### 4.2.2.1. *Description of Model 9*

Model 9 consists of two blocks. These blocks are placed at different depths, as shown in Figures 33-34, with an anomalous density of 1.0 $\mathrm{g/cm^3}$. The observed vertical gravity field data are displayed in Figure 35.

4.2.2.2. *Inversion Result*

I have tested the developed inversion algorithms based on CRRCG and RCG methods to compare the results with the true model parameters.

4.2.2.2.1. Inversion without constraints and focusing. As for Model 4, I first applied the unconstrained and unfocused inversion algorithm. The result is shown in Figures 36 and 37. One can see that inversion with RCG method was capable of finding the true models' locations with 60% true density recovery; however, there is still a problem with detection of the bottom part of the anomalous bodies (see Figure 37).

4.2.2.2.2. Inversion with constraints and focusing. In the second set of numerical experiments for Model 9, we set the density constraints, boundaries of the logarithmic space transformation, to be symmetric, e.g., $-1\frac{g}{cm3} \leq m_i \leq 1\frac{d}{cm3}$. Figure 38 presents the plots of the relative misfit, parametric functional, and stabilizer versus the iteration number, observed gravity field, and predicted gravity field data for constrained and focused inversion. The results of the constrained and focusing (reweighted) inversion, shown in Figure 39, demonstrate that the algorithm is capable of recovering the true model location and the anomalous density distribution, especially with the inverse model of the shallower body perfectly matching the true block location (see Figure 39).

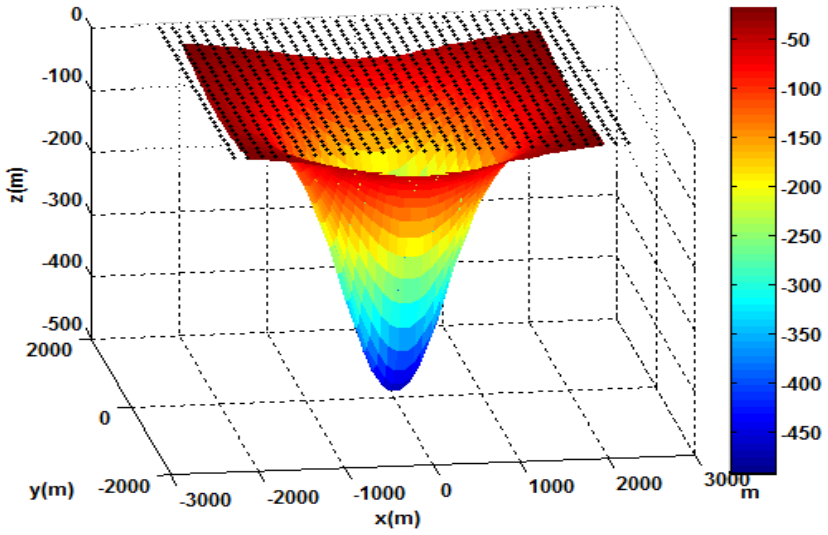


Figure 5: Model 1 of the sediment-basement interface. Black dots represent the observation points.

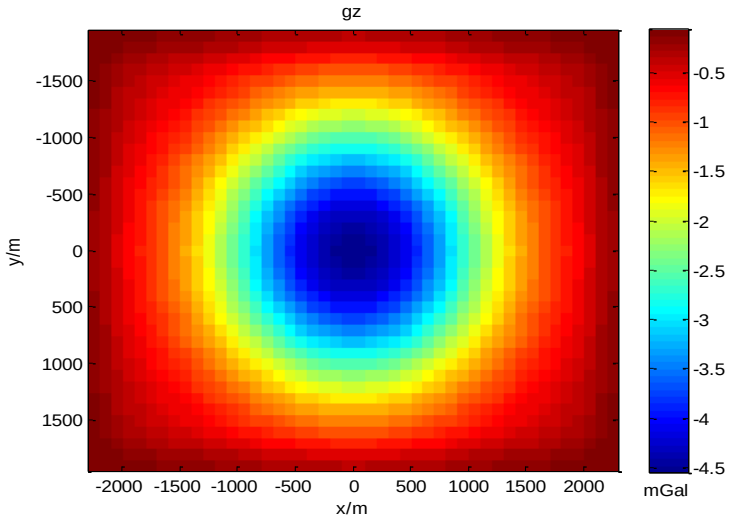


Figure 6: Model 1: Observed gravity field data.

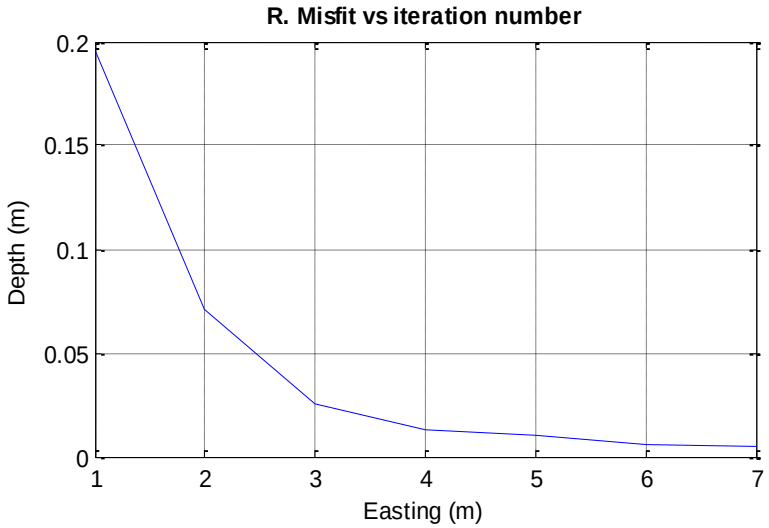


Figure 7: Model 1: Relative misfit values versus iteration.

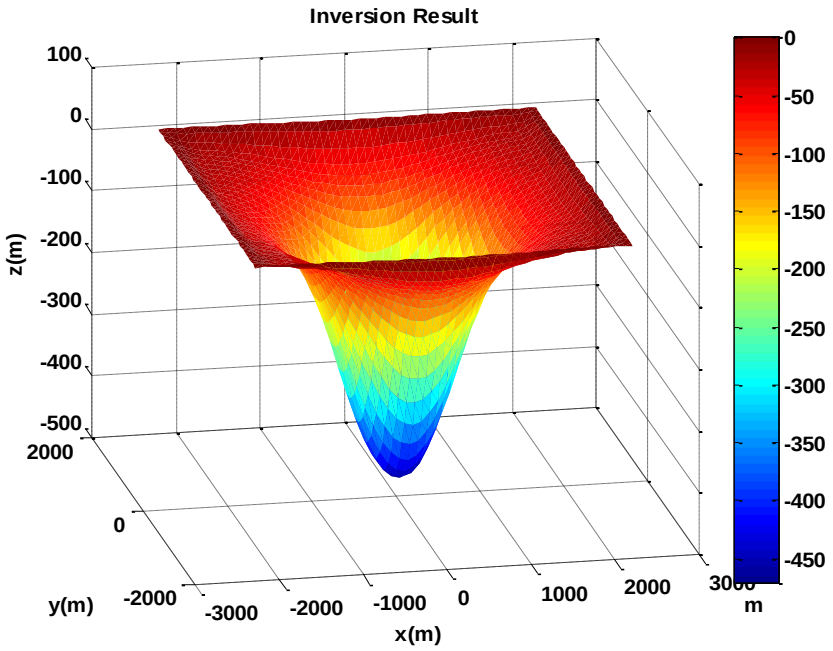


Figure 8:  Model 1: Inversion result.

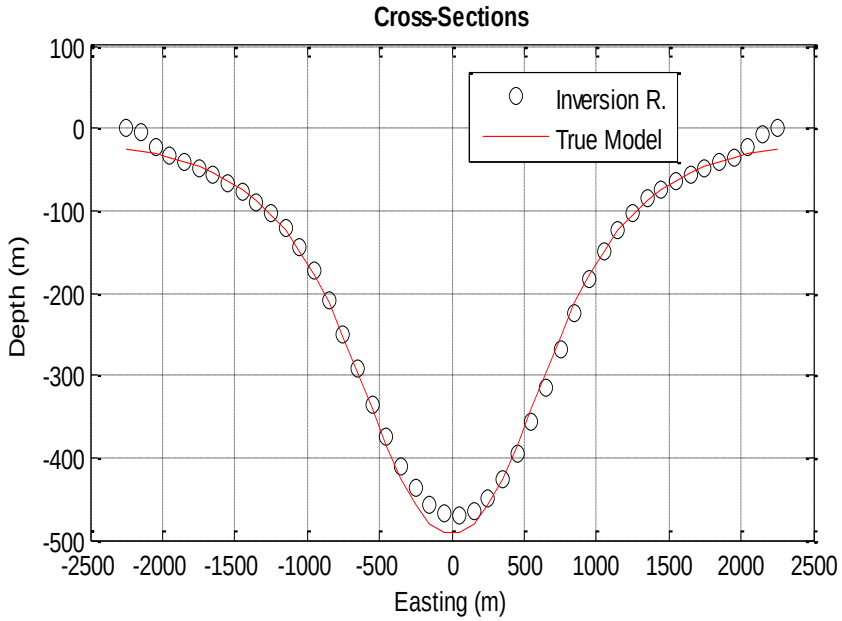


Figure 9: Model 1: Cross sections of the true model and the inversion result.

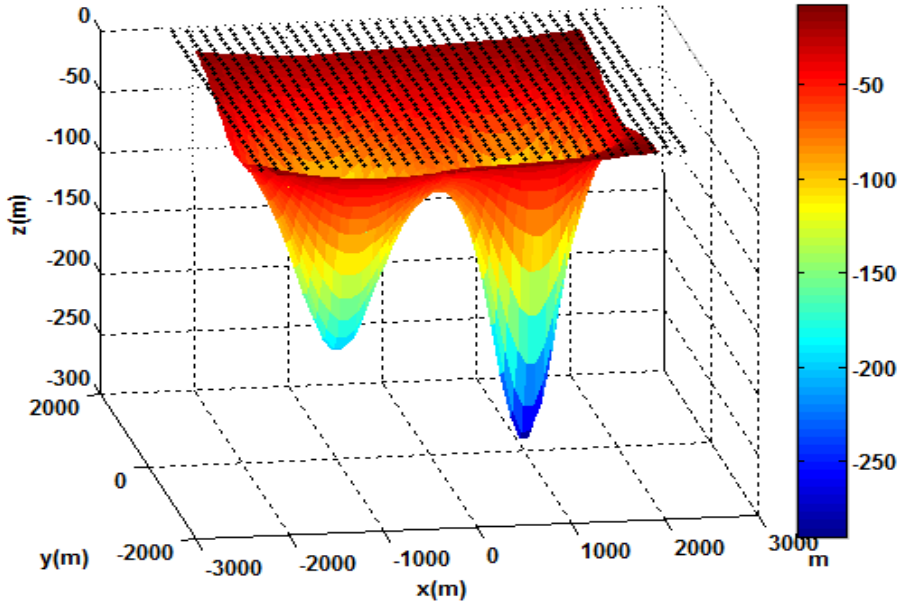


Figure 10: Model 2 of the sediment-basement interface with two dips.

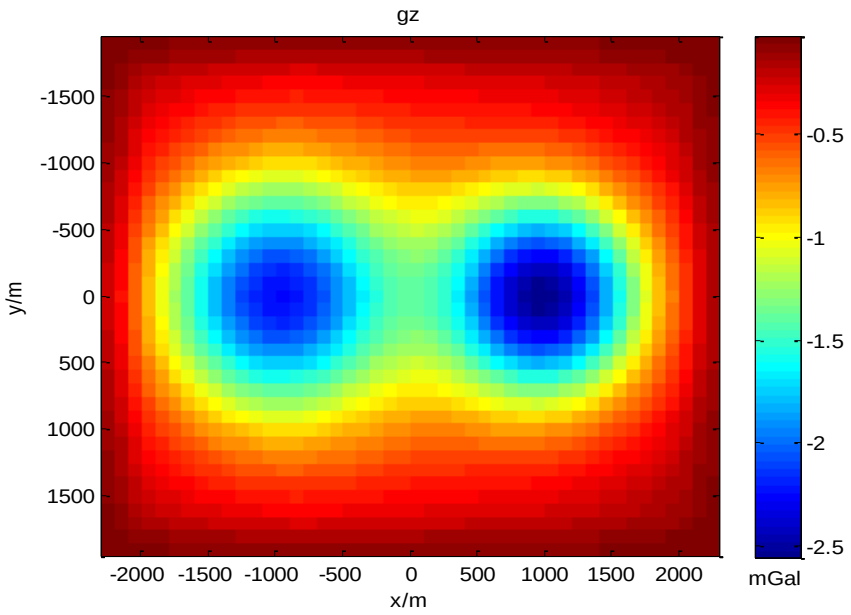


Figure 11: Model 2: Observed gravity field data.

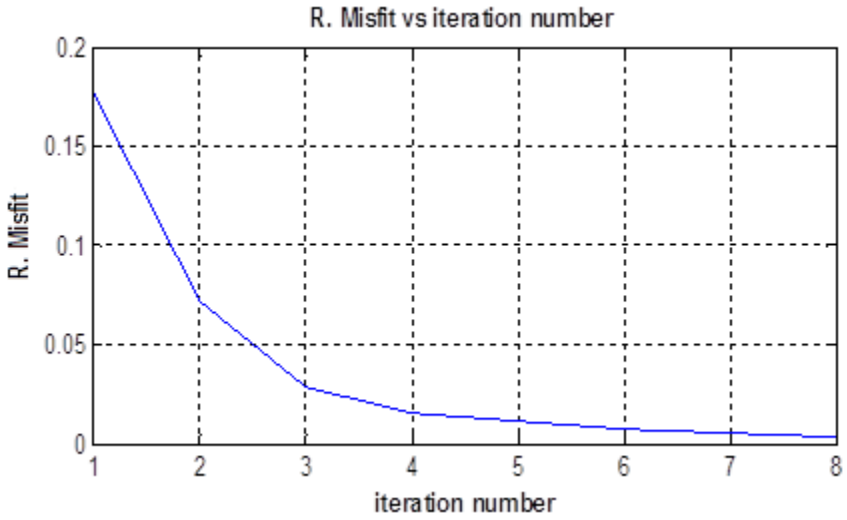


Figure 12: Model 2: Relative misfit values versus iteration.

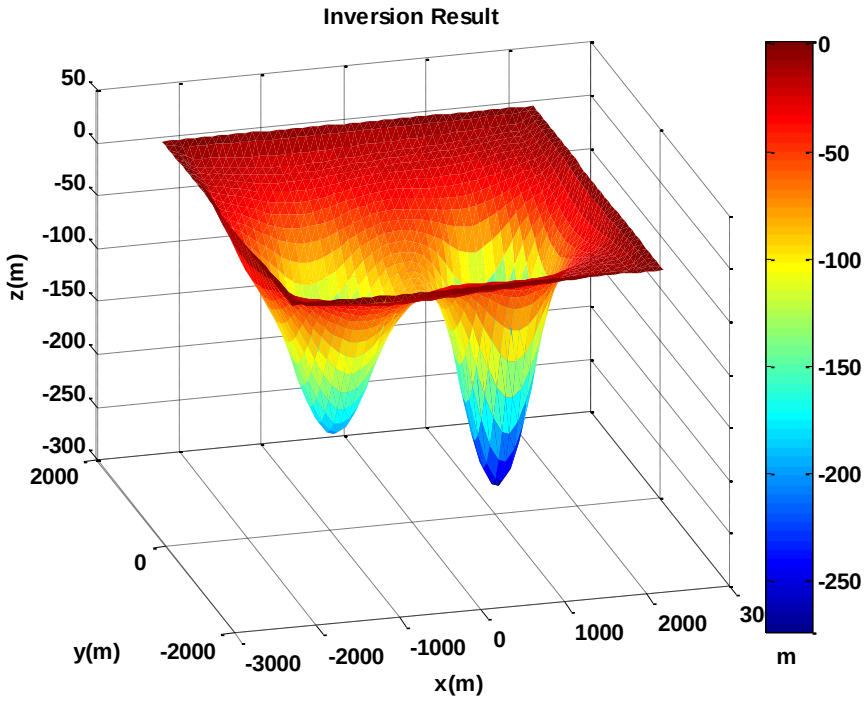


Figure 13: Model 2: Inversion result.

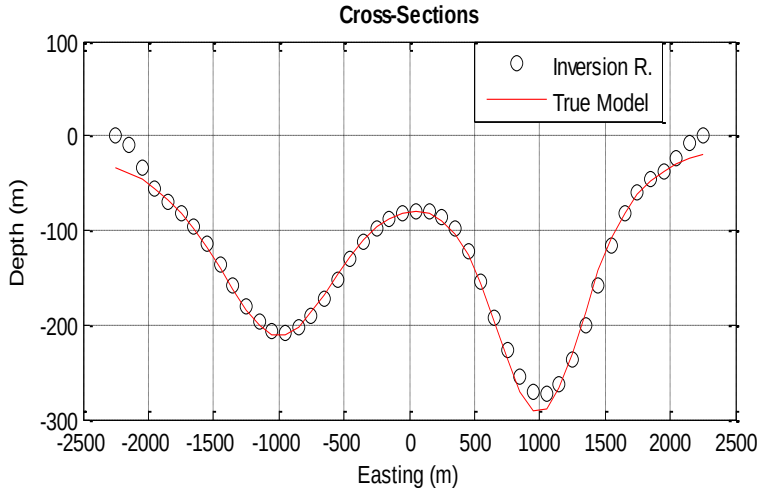


Figure 14: Model 2: Cross sections of the true model and the inversion result.

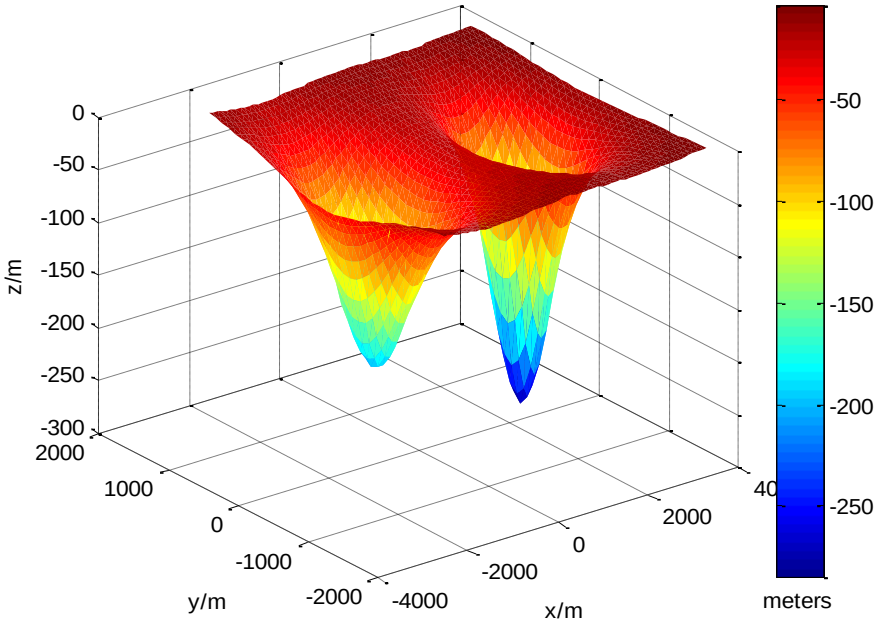


Figure 15: Model 3 of the sediment-basement interface with a poor coverage.

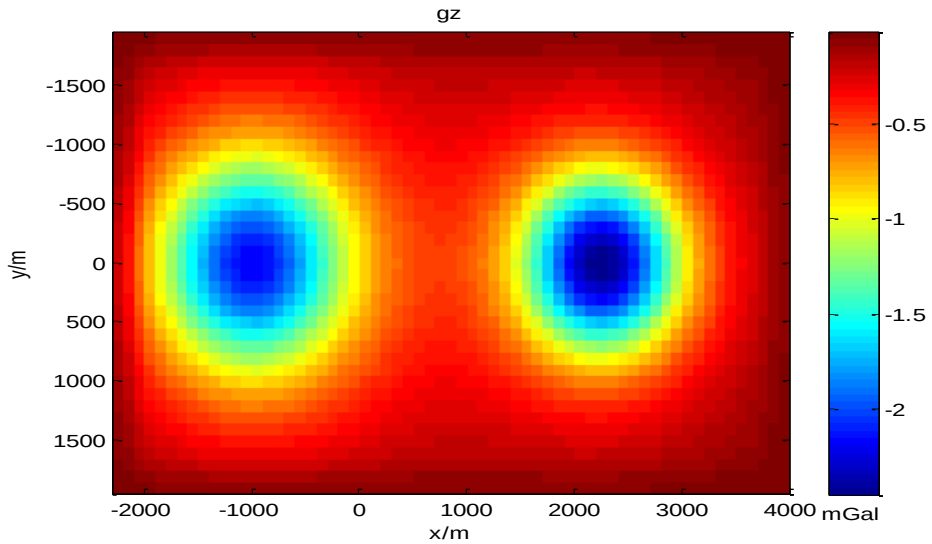


Figure 16: Model 3: Observed gravity field data.

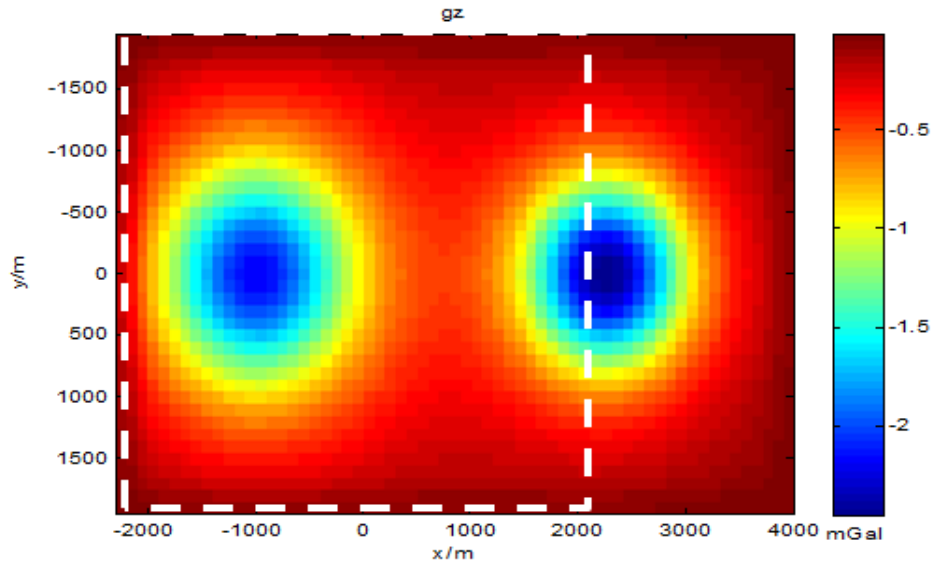


Figure 17: Model 3: Observed gravity field data with a white dashed rectangle indicating the area of the data used for inversion.

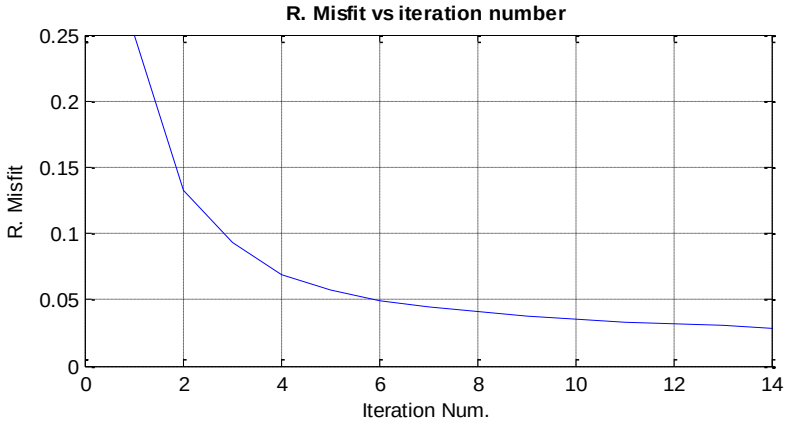


Figure 18: Model 3: Relative misfit values versus iteration number.

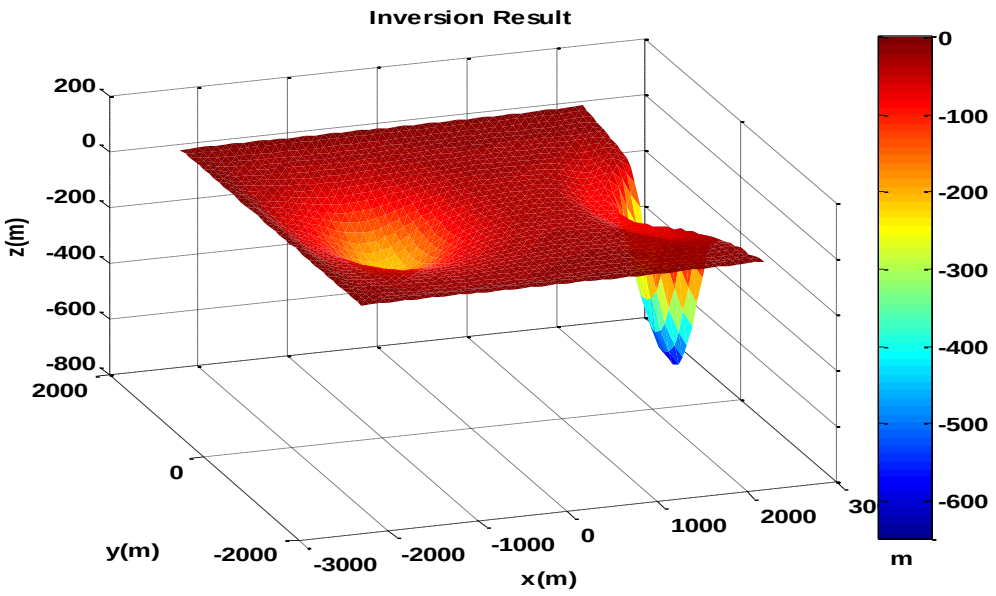


Figure 19:  Model 3: Inversion result.

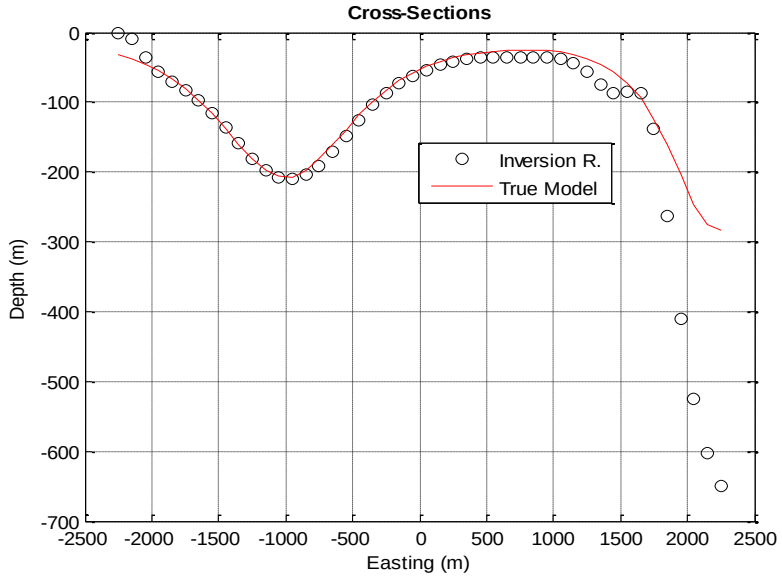


Figure 20: Model 3: Cross sections of the true model and the inversion result.

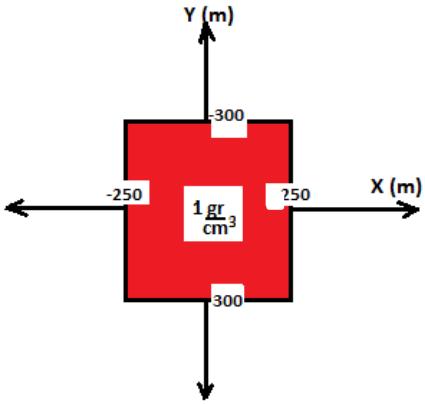


Figure 21: Model 4: Plane view.

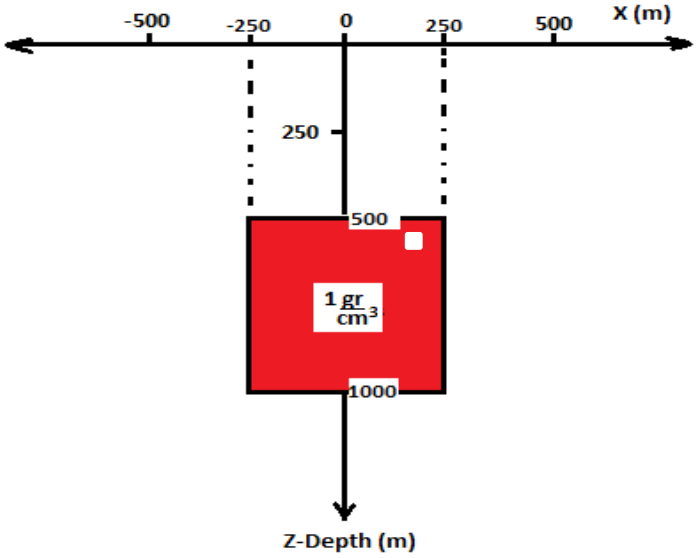


Figure 22: Model 4:  Vertical section.

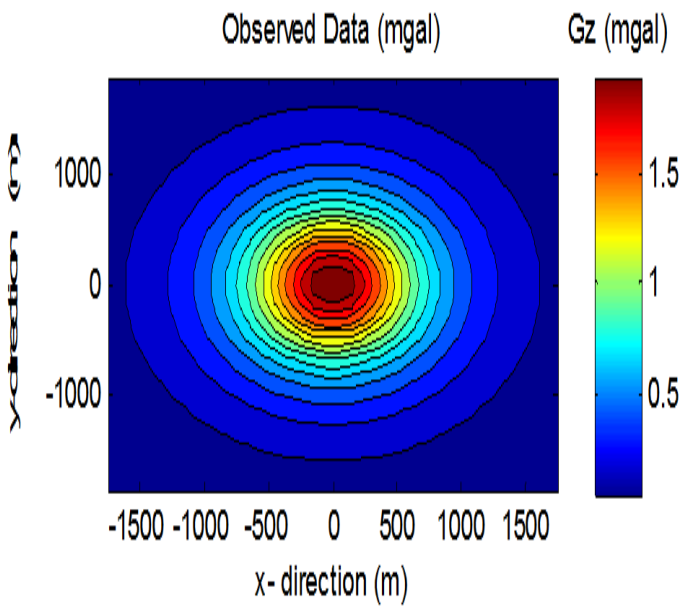


Figure 23: Model 4: Observed gravity field.

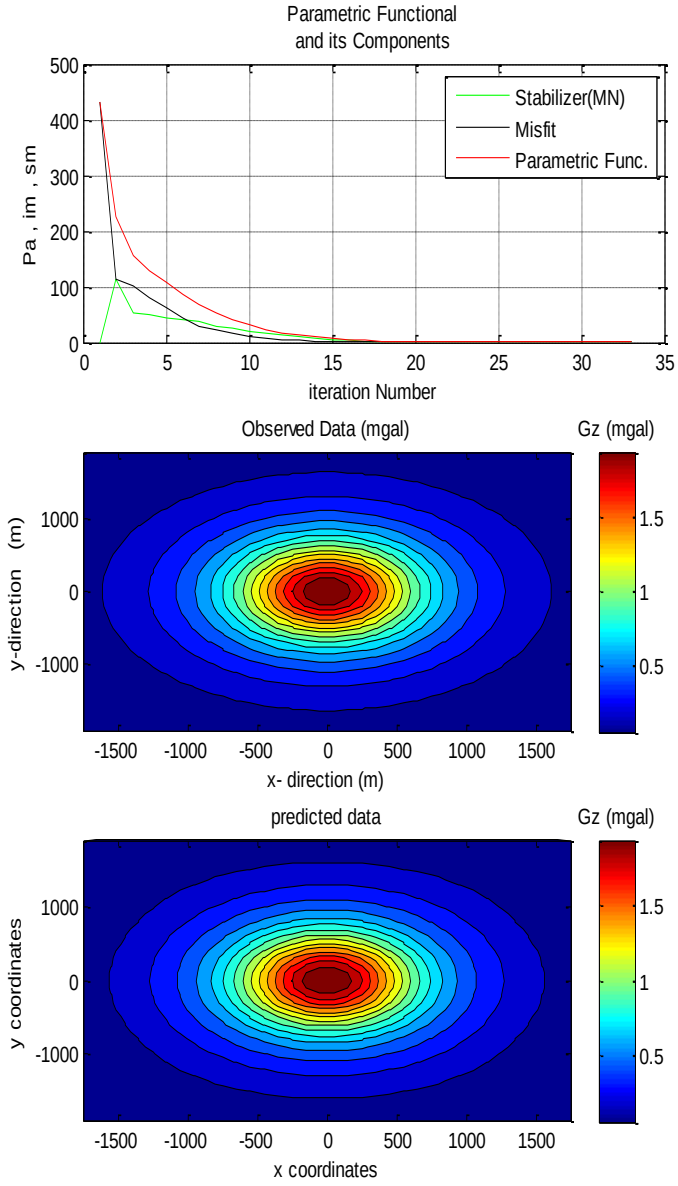


Figure 24: Model 4: Relative misfit, parametric functional, and stabilizer versus the iteration number (top panel), observed gravity field (middle panel), and predicted gravity field (bottom panel) for unconstrained and unfocused inversion.

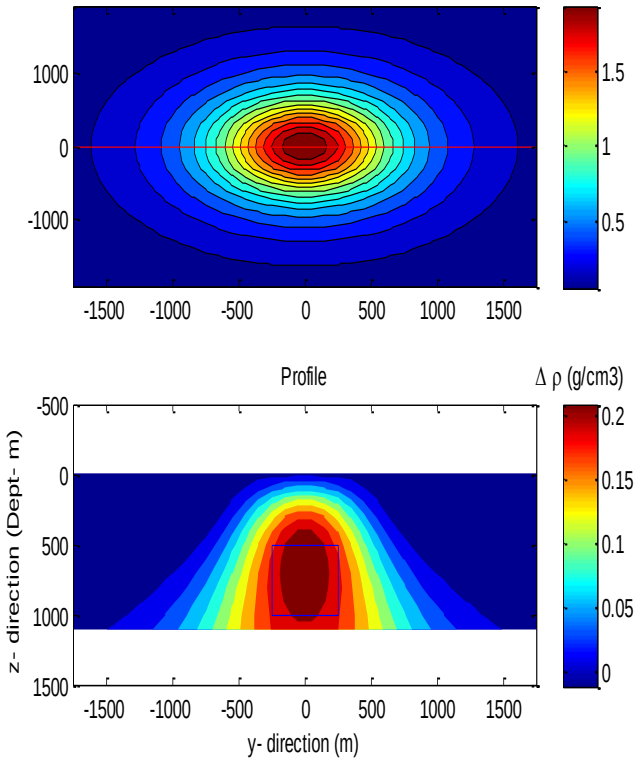


Figure 25: Model 4: Horizontal (top panel) and vertical (bottom panel) cross sections of the inversion result for unconstrained and unfocused inversion. A blue rectangle shows the true model with the density contrast of $1.0\ g/cm^3$.

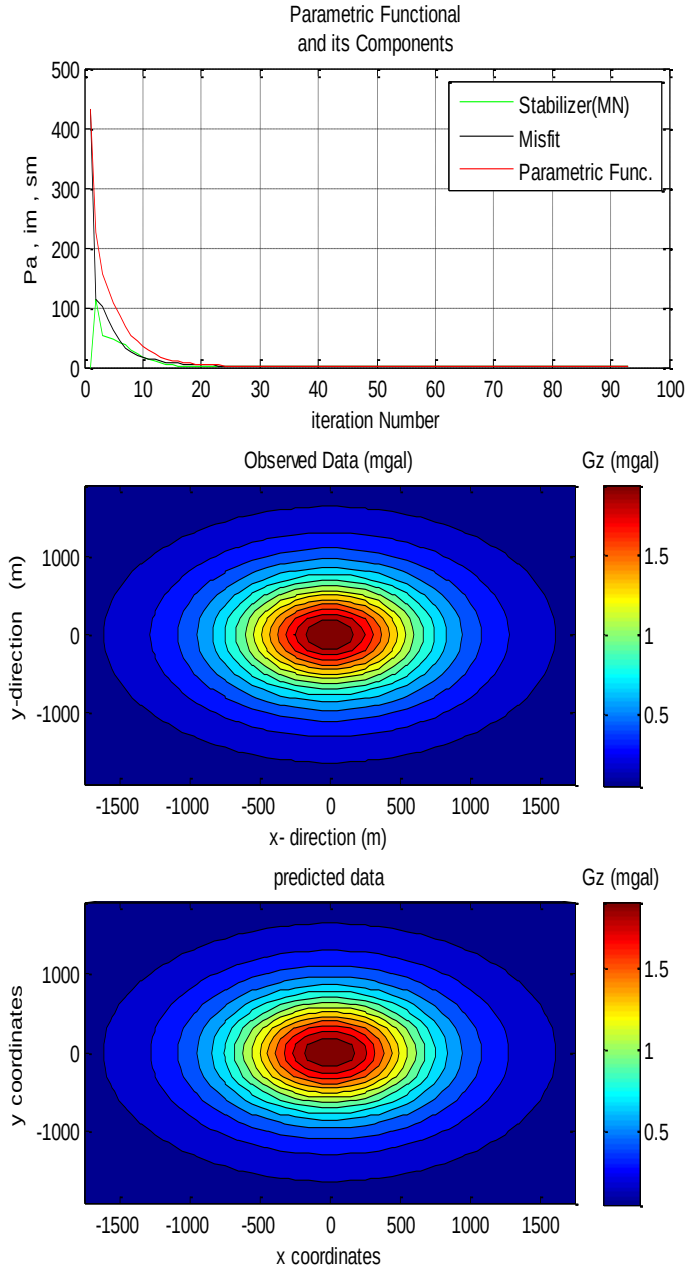


Figure 26: Model 4: Relative misfit, parametric functional, and stabilizer versus the iteration number (top panel), observed gravity field (middle panel), and predicted gravity field (bottom panel) for constrained and focused inversion.

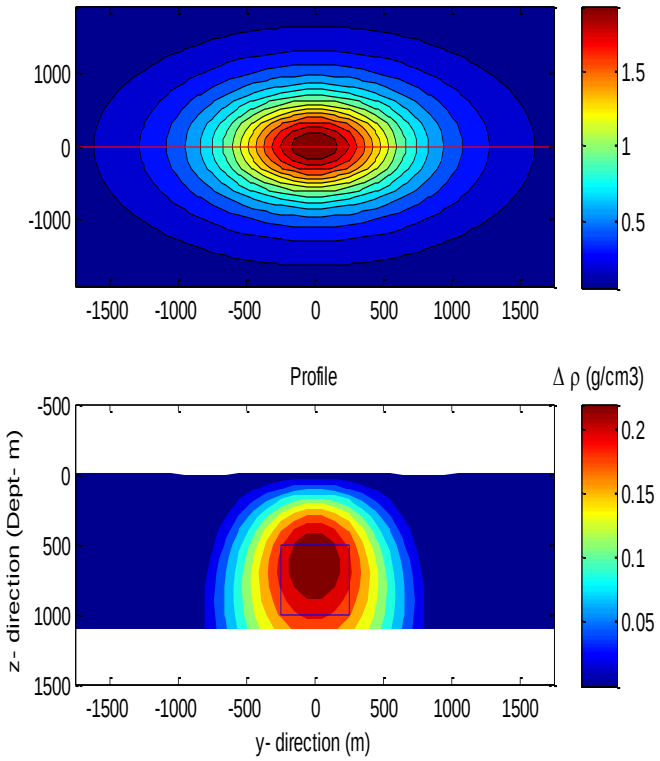


Figure 27: Model 4: Horizontal (top panel) and vertical (bottom panel) cross sections of the inversion results for constrained and focused inversion. A blue rectangle shows the true model with the density contrast of $1.0\ g/cm^3$.

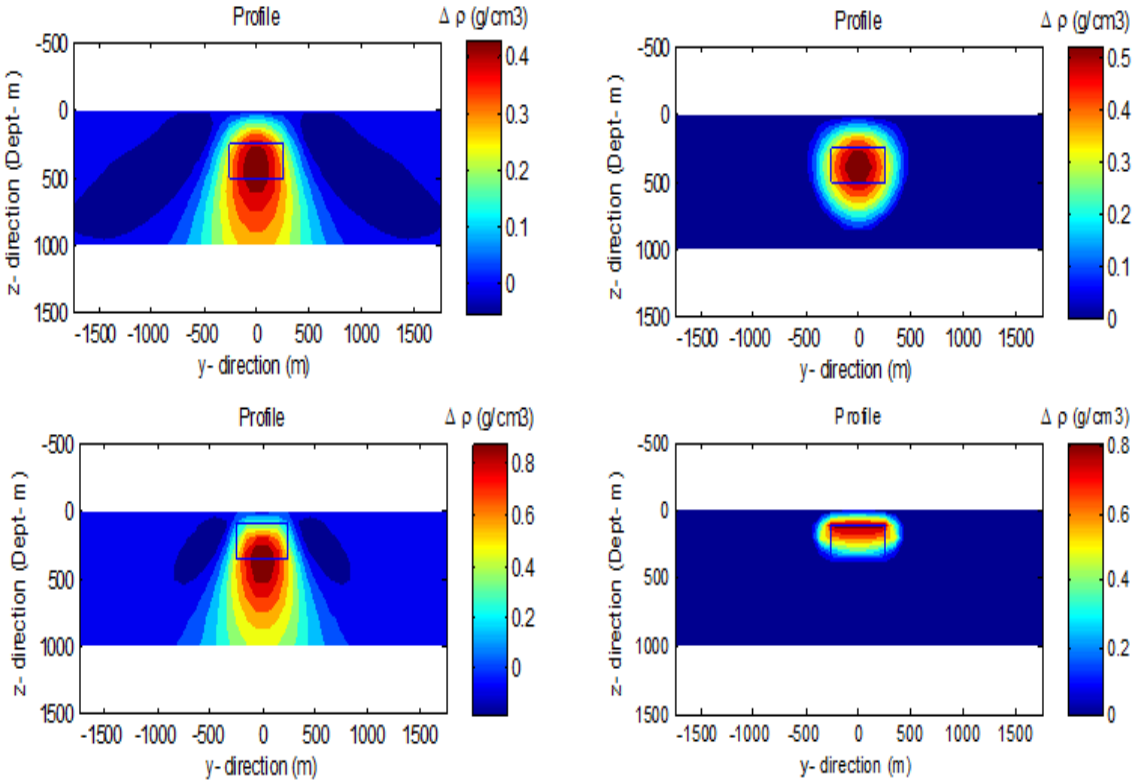


Figure 28: Models 5 (top panels) and 6 (bottom panels): A blue rectangle shows the true model with the density contrast of $1.0\ g/cm^3$. The results of unconstrained and unfocused inversion are shown on the left, while the inverse models obtained by the constrained and focused inversion are plotted on the right.

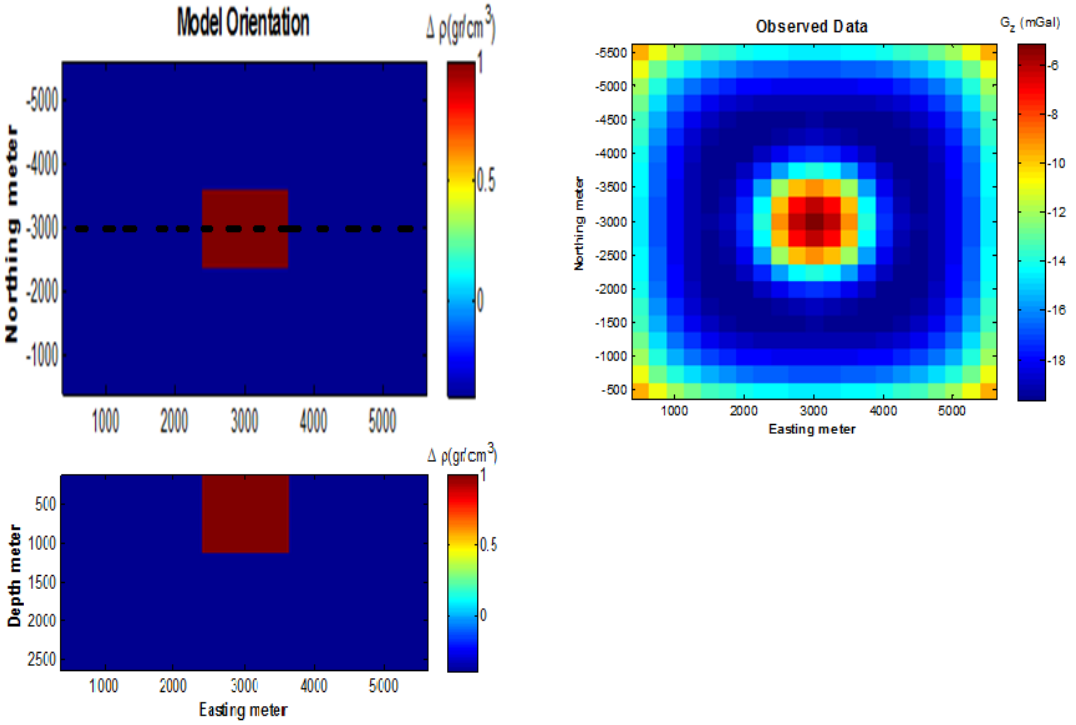


Figure 29: Model 7: Left panels show the horizontal and vertical sections of the anomalous body placed within a homogenous half space with a density of $-0.4\ g/c$. A black dashed line is the location of the profile for the vertical cross section. The right panel shows the observed data.

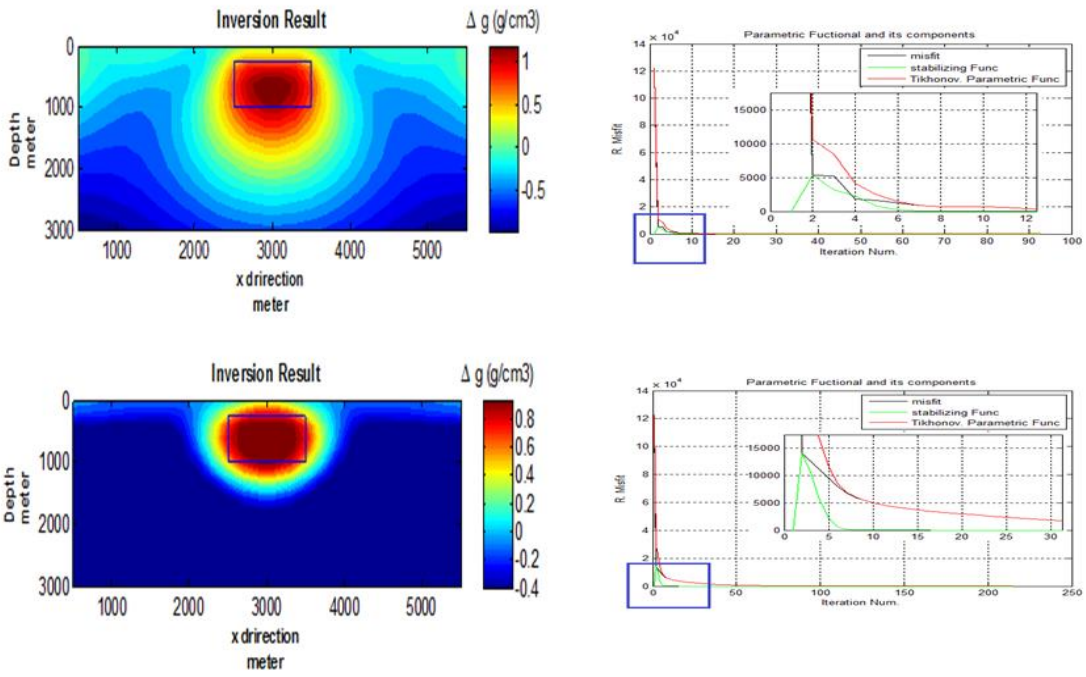


Figure 30: Model 7: The left panels show the vertical sections for the inversion results; the top panel presents the unconstrained and unfocused inversion, while the bottom panel shows the constrained and focused result. The corresponding plots of the relative misfit, parametric functional, and stabilizer versus the iteration number are shown on the right.

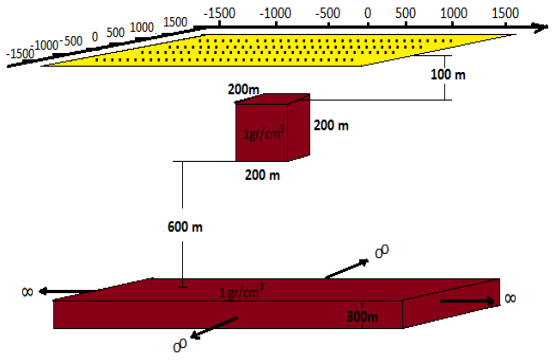


Figure 31: Model 8 with a single block and a basement-like structure.

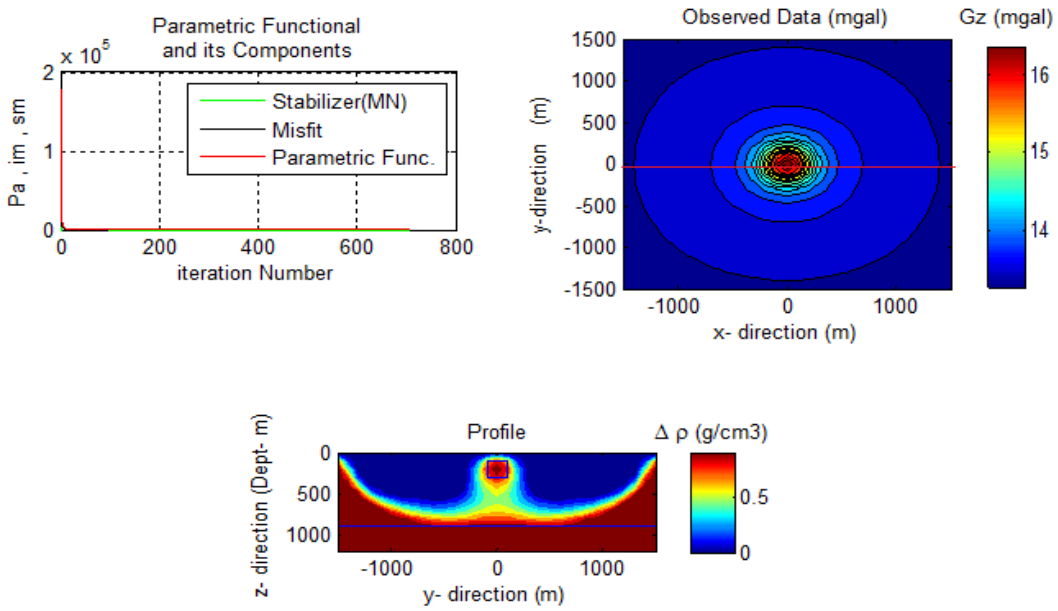


Figure 32: Model 8: Relative misfit, parametric functional, and stabilizer versus the iteration number (top left panel) and the observed gravity field (top right panel. The bottom panel shows a vertical section of the inversion result taken along the profile shown in the top right panel.

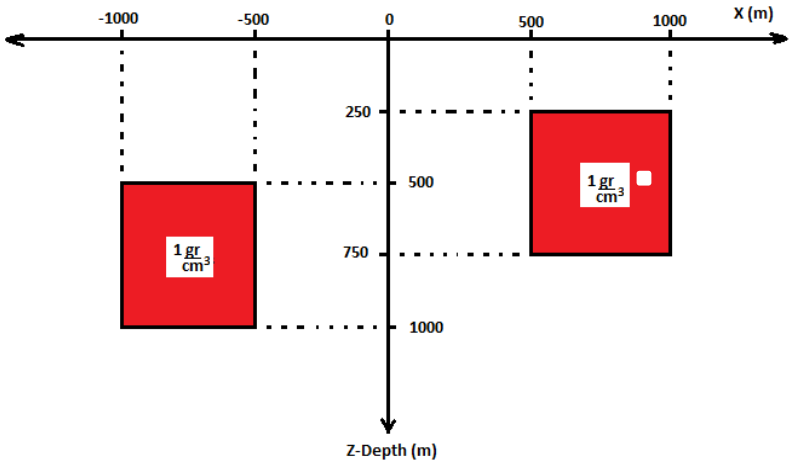


Figure 33: Model 9: Plane view.

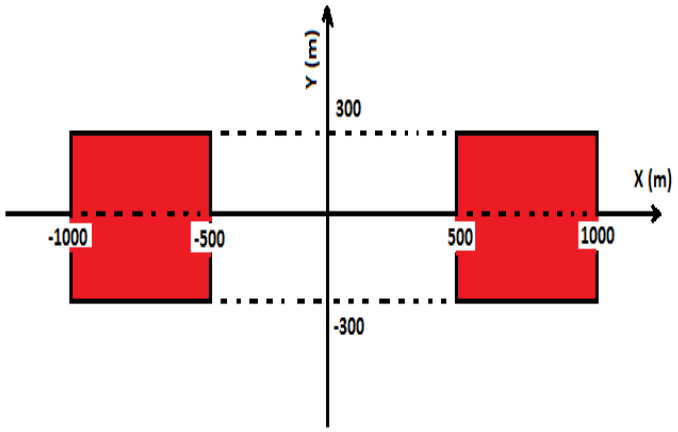


Figure 34: Model 9: Vertical section.

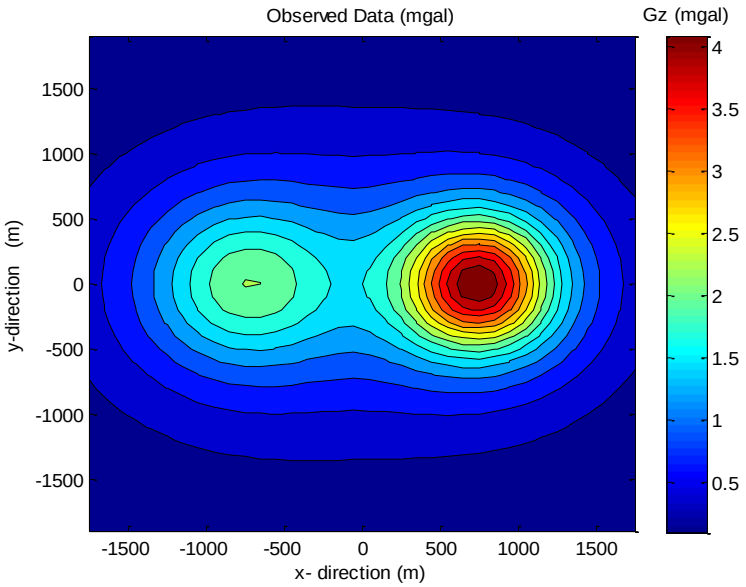


Figure 35: Model 9: Observed gravity field.

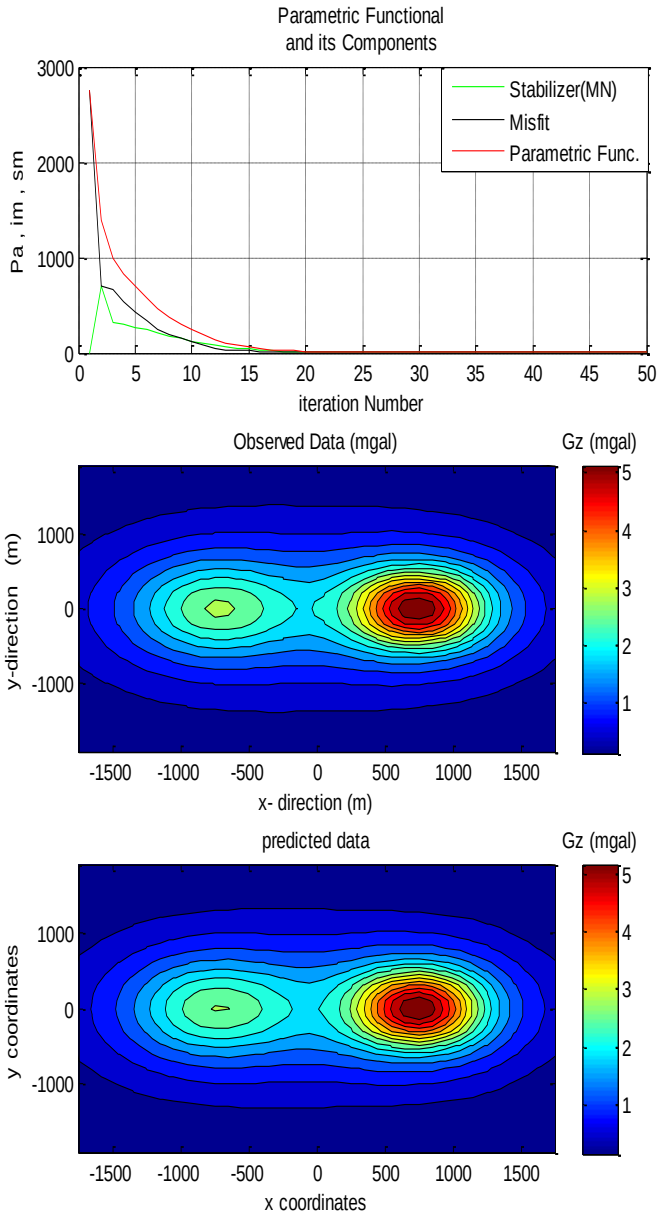


Figure 36: Model 9: Relative misfit, parametric functional, and stabilizer versus the iteration number (top panel), observed gravity field (middle panel), and predicted gravity field (bottom panel) for unconstrained and unfocused inversion.

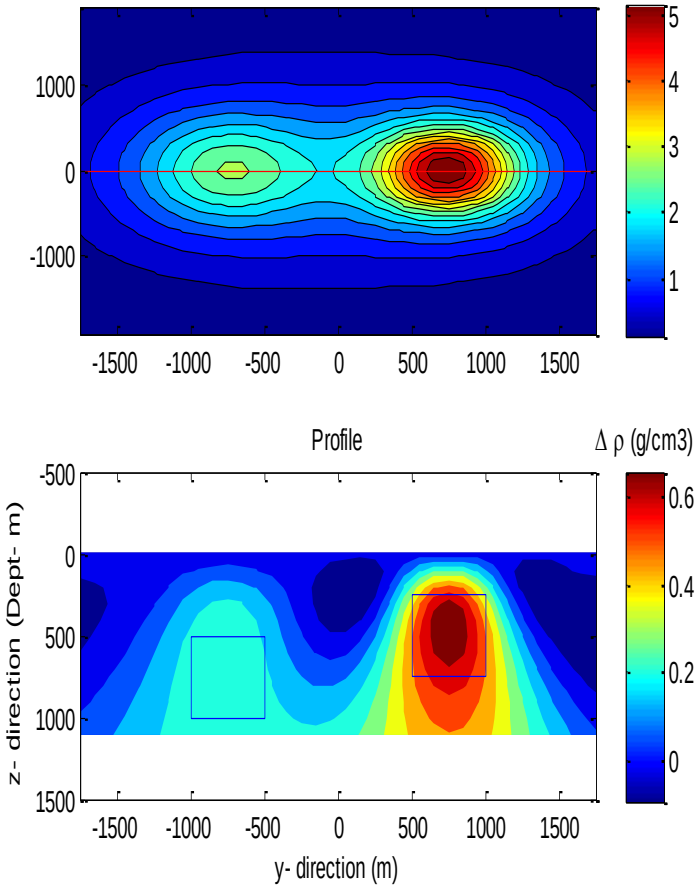


Figure 37: Model 9: Horizontal (top panel) and vertical (bottom panel) cross sections of the inversion result for unconstrained and unfocused inversion. Two blue rectangles show the true location of the blocks with the density contrast of 1.0 $g/cm^3$.

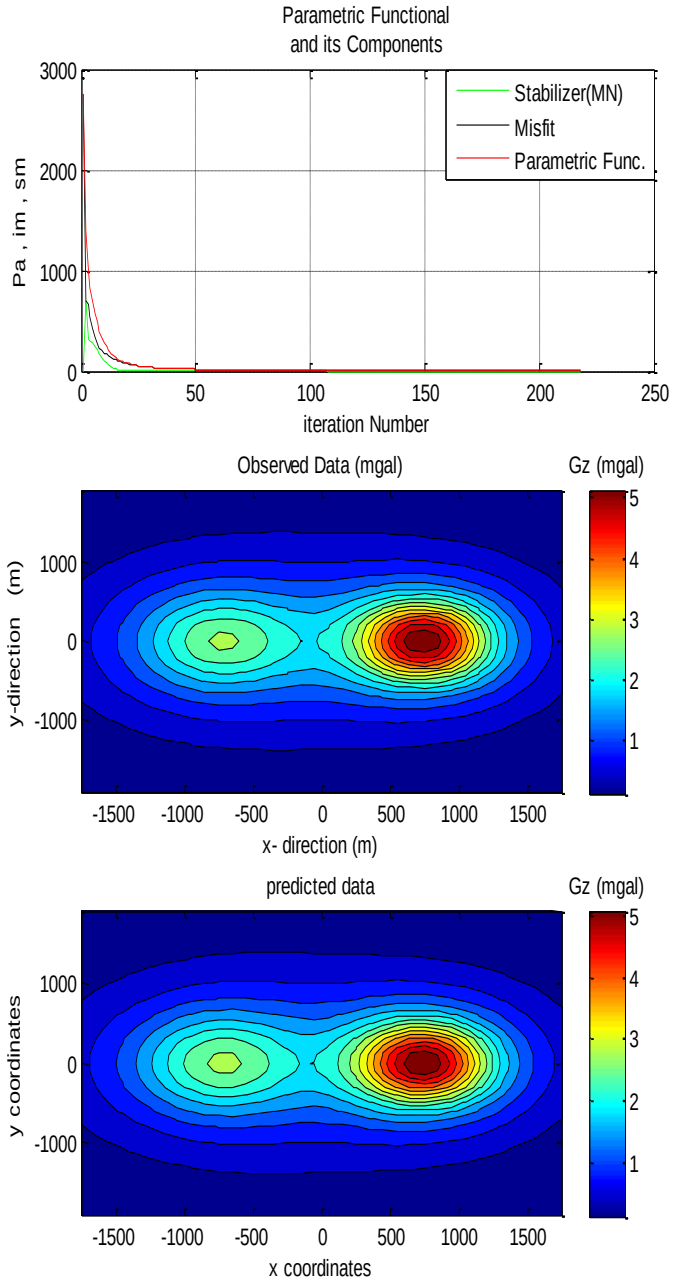


Figure 38: Model 9: Relative misfit, parametric functional, and stabilizer versus the iteration number (top panel), observed gravity field (middle panel), and predicted gravity field (bottom panel) for constrained and focused inversion.

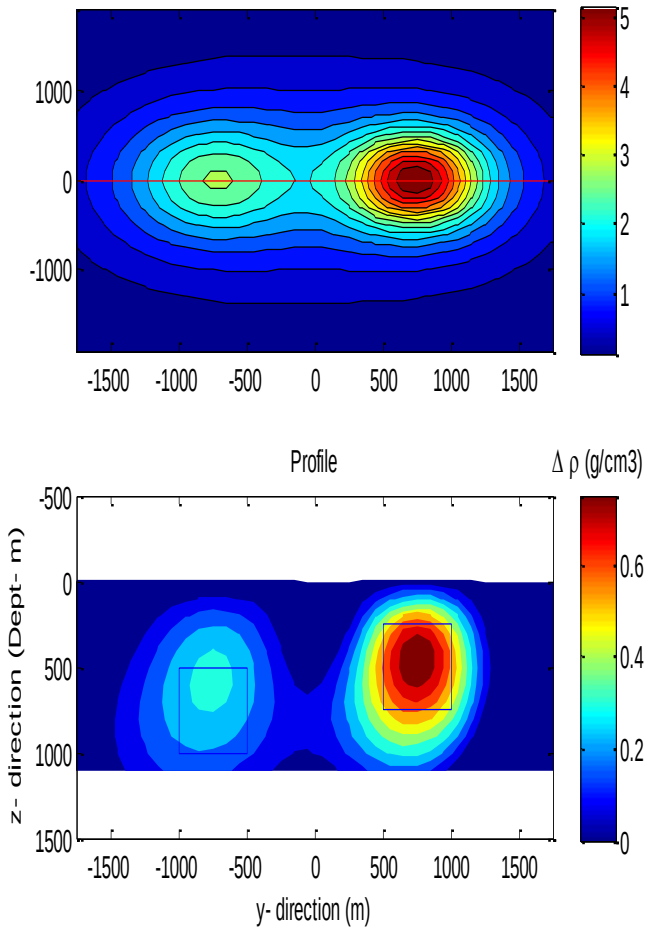


Figure 39: Model 9: Horizontal (top panel) and vertical (bottom panel) cross sections of the inversion results for constrained and focused inversion. Two blue rectangles show the true model with the density contrast of 1.0 $g/cm^3$.

# CHAPTER 5

# CASE STUDY: SURPRISE VALLEY (NE CALIFORNIA/NW NEVADA)

## 5.1. Geography

Surprise Valley is located in northeastern California and western Nevada. The valley extends in the north-south direction for about 50 miles, and in the east-west direction up to 12 miles. The elevation ranges up to 4,500 feet at the highest point (see Figure 40). Surprise Valley is geographically separated into three parts, Upper Lake, Middle Lake, and Lower Lake.

## 5.2. Geology

Surprise Valley is generally bounded by Warner Range to the west and Hays Canyon Range to the east. The area has also been marked by Surprise Valley Fault (SVF) and Hays Canyon Fault (HCF) to the west and east, respectively. A full graben is created by Hays Canyon Fault on the western margin of the valley. SVF is the most prominent structure in the area, and it has a vertical displacement up to 5,000 feet on the east side of Warner Range. The other noticeable feature within the valley is Lake City Fault (LCF), which begins from the northwestern margin to southeastern margin of the valley. The area between Warner Range and Hays Canyon range marks a transition from an

extensional Basin and Range to an extensional Modoc Plateau (Ponceet al., 2009). Since the study by Hedel (1984) the area became a subject of geological and geophysical investigations due to its potential and complex geological settings (e.g., Lerch et al., 2006; Glen et al., 2008; Egger et al., 2009; 2014; and Lerch et al., 2009).

In this study, I have used the isostatic gravity data with the removed regional effect to determine the anomalous density distribution in the subsurface of the valley. Both the unconstrained inversion and constrained inversion with focusing were used to compare the results.

I have also used the same gravity field data to estimate the depth of the basin using the Cauchy-type integral method (Cai and Zhdanov, 2014). The results were compared with other studies, such as Egger et al. (2009a; 2009b 2010), Lerch et al. (2007), and Colgan et al. (2008). However, neither of the cited papers presents a clear depth to the basement for either a part of or the entire valley. There were several attempts to solve the depth-to-basement estimation problems using a conventional volume discretization method over decades. However, with the conventional method, one needs to divide the subsurface into many small prisms which requires significant computational resources and time. Thanks to the advanced depth-to-basement estimation method based on the Cauchy-type integral introduced by Cai and Zhdanov (2014), this 3D problem can be reduced to much more economic surface integration.

## 5.3. Geophysical Properties

### 5.3.1. Rock Samples

Rock samples were collected by USGS with geographic coordinates (NAD27). Additional rock samples were taken from a drill-hole drilled by AMP Resources. The samples from the drilling hole indicate many intrusive volcanic dense formations in the subsurface of the valley (Ponce et al., 2009). The density of the rock samples on the surface around the area were taken into account for basement outcrop interpretation (see Figure 41). Note that, due to the presence of intrusive volcanic rocks, seismic data were not able to provide a clear picture of the sediment-basement interface (Egger et al., 2010).

### 5.3.2. Gravity Data

The gravity survey was conducted by using a LaCoste and Romberg gravimeter G614 and a Scintrex CG-5 gravimeter. The total number of the data point was 3,784 (Figure 42). All required gravity corrections were applied, including: (a) Earth-tide correction, which corrects for the tidal effects of the moon and sun; (b) instrument-drift correction, which compensates for the drift in the instrument's spring; (c) latitude correction, which accounts for the variation of the Earth's gravity field with latitude; (d) free-air correction, which accounts for the variation in gravity due to elevation relative to the sea level; (e) Bouguer correction, which corrects for the attraction of material between the station and the sea level; (f) curvature correction, which corrects the Bouguer correction for the effect of the Earth's curvature; (g) terrain correction, which removes the effect of topography to a radial distance of 167 km around the station; and (h) isostatic

correction, which removes long-wavelength variations in the gravity field related to the compensation of topographic loads (Credit: USGS, Ponce et al., 2009).

## 5.4. Inversion for the Basement Using Cauchy-type Integral Method

### 5.4.1. Data Processing

In this part, I use gravity field data to estimate the thickness of the basin using the depth-to-basement estimation method based on the Cauchy-type integral (Cai and Zhdanov, 2014). According to USGS, the central part of the valley, filled with the low-density alluvial and volcanic deposits, has the depth of approximately 1.5 km corresponding to 20 mGal gravity with 0.4 $\mathrm{g/cm^3}$ density contrast (Ponce et al., 2009). Egger et al. (2010) used seismic and potential field data to define subsurface geology of the upper part of Surprise Valley. According to their forward modeling, they could reach a depth of approximately 1.5 km (Egger et al., 2010). In addition to these papers, another study from Egger et al. (2009) stated that ray-trace modeling of direct and refracted arrivals confirmed 1.5 km depth of basin.

For the depth-to-basement estimation, isostatic gravity data were used (Bonini, 1965), because isostatic gravity data represent changes in the crust only. However, isostatic gravity data may still carry some gravity effect from the basement at high elevation due to uplifting. In such cases, it is suggested to subtract an isostatic basement component from the total isostatic gravity data. I have used a number of observation stations located in the points that can be interpreted to be the basement outcrops, where I assume that the gravity values represent the effect of the basement only. After this step, a residual isostatic

gravity map shows the gravity field caused by sediment deposits over the basement only.

Figure 43 presents the isostatic map with regional effect, while Figure 44 represents the isostatic effect from the basement. The regional field is plotted using some observation stations located on the basement's outcrops.

### 5.4.2. Inversion Results

I have applied the depth-to-basement estimation algorithm to the gravity data collected over a selected area shown by a black rectangle over the isostatic gravity map. The map of the basin of the isostatic gravity field over the target area is shown over the topographic map. The inversion domain was divided into the vertical prisms with a horizontal size of 500 m x 500 m in the x and y directions and a density contrast of $0.4\mathrm{g/cm}^3$. The inversion was terminated when the elative misfit reached 5 %. I could try to run the inversion to a lower misfit level; however, artificial effect could be generated in that case due to poor data coverage in the northwest and southeast parts of the study area. The map of the observe gravity data, relative misfit versus iteration number, and the predicted gravity data is shown in Figure 45, 46, and 47, respectively.

Figure 48 presents the inversion result obtained using the depth-to-basement estimation based on the Cauchy-type integral, and Figure 49 presents a map of absolute differences between the observed and predicted data. Due to poor data coverage in the sides on the inversion domain, one can see an increase in the difference values on the edges. Thus, one needs to define the

area where we can expect a more reliable inversion result. This area is outlined by the red rectangle in Figure 49.

In Figure 50, I present the results of interpretation of the depth to the basement produced from seismic and gravity data by Egger et al. (2010) over the seismic cross section, which corresponds to the green profile limited by a white rectangle in Figure 51. The dashed line shows the limit of the reversed ray coverage (after Egger et al., 2010). The red line represents the depth to the basement interpreted based on seismic data. The green line shows the inversion result obtained using the depth-to-basement estimation based on the Cauchy-type integral.

Figure 52 presents vertical cross sections of the recovered depth to the basement taken along three profiles indicated by black, green, and white lines in the inversion result, respectively. In the area indicated by a red rectangle, the middle profile with the maximum depth of 2000 m perfectly matches the cross section produced by the joint seismic-gravity interpretation result from Egger et al. (2010).

## 5.5. Inversion for 3D Subsurface Density Distribution Using the Volume Integral Method

I have applied the 3D inversion method based on the volume integrals to the same basin isostatic data, which were used for the depth-to-basement inversion. The inversion domain was divided into cells that have size of 500 m x 500 m x 500 m in the x, y, and z directions, respectively. As it was demonstrated

by the model study, it is critical to use the constrained and focused inversion in order to produce the image of the sediment-basement interface. Therefore, I have applied the constrained and focused inversion code to the observed basin isostatic data.

Figure 53 presents a plot of the relative misfit vs. the iteration number. The inversion was terminated when the elative misfit reached 5 %. The density model obtained by this inversion is shown in Figures 54 and 55. From inversion results, it is clear that inversion was able to recover a basement reasonably enough. In the west part of the basin, the basement part is clearly displayed with dark brown color; however, the east part of the inversion result is produced with deeper structure with less dense formation relative to the west. In order to make further interpretation for the result, I will compare density distribution with depth-to-basement estimation results obtained by the method based on the Cauchy-type integral. The top section in Figure 56 shows some anomalous structures below the estimated surface of the basin, which may be related to the internal blocky structure of the basement. In order to conduct this comparison, I have superimposed the vertical sections of inverse models produced by both methods along the profiles shown in Figure 56. It is important to compare these results jointly with the known geology to better define the possible structure of the sediment-basement interface. The vertical sections along these three profiles are shown in Figure 57. The yellow arrows indicate outcropping of the basement on the ground. The solid black lines show the sediment-basement interface determined by the surface Cauchy-type integral method. One can see that the

volume density distribution is well consistent with the results from the Cauchy-type integral method.

The inversion results are relatively consistent with the known geology. Indeed, both methods (Figure 57) show basement outcrops at the same locations on the ground, where they are present according to known geology (indicated by the yellow arrows).

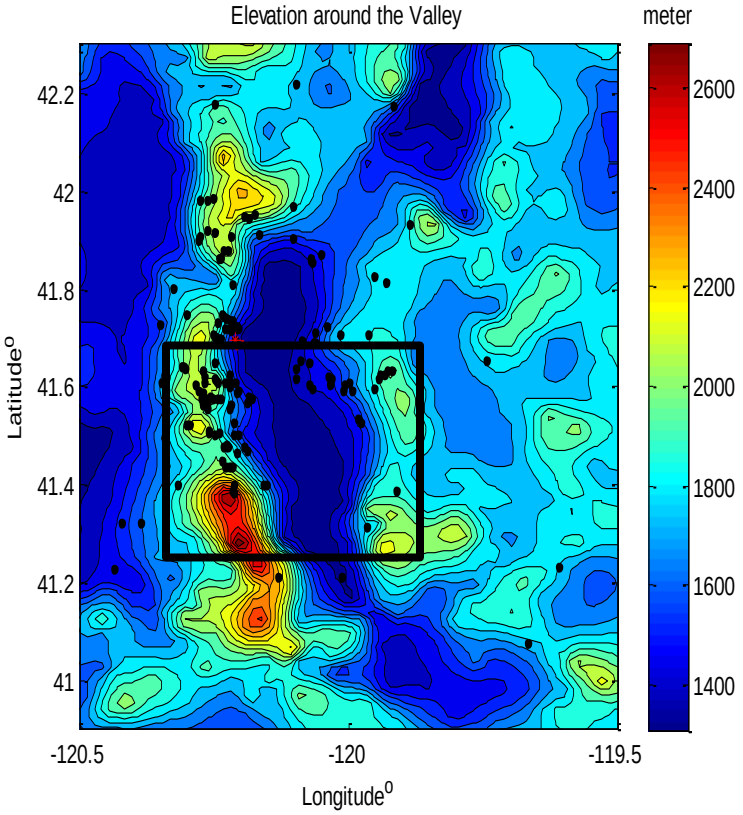


Figure 40: Topographic elevation in Surprise Valley and adjacent areas. The black dots show the locations of the rock samples, red stars indicate the drill-hole LCSH-05 location. The black rectangular indicates the area of interest for depth-to-basement estimation.

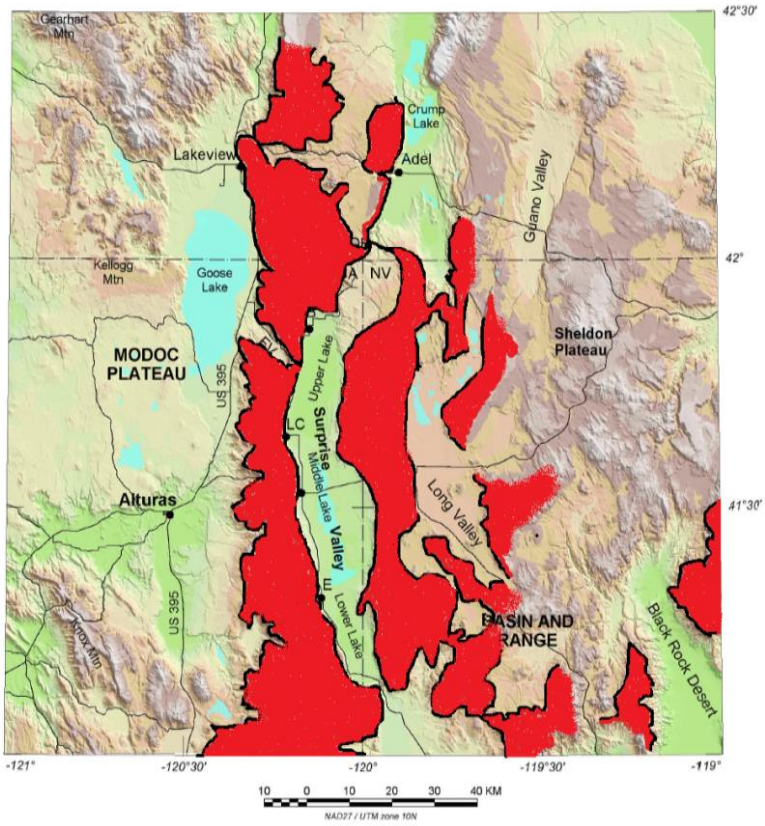


Credit: U.S. Geological Survey Department of the Interior/USGS
https://pubs.usgs.gov/of/2009/1157/of2009-1157.pdf

Figure 41: Topographic map (after Egger et al., 2009) with basement outcrops indicated with red areas interpreted based on rock samples, elevation, and gravity values at observation points.

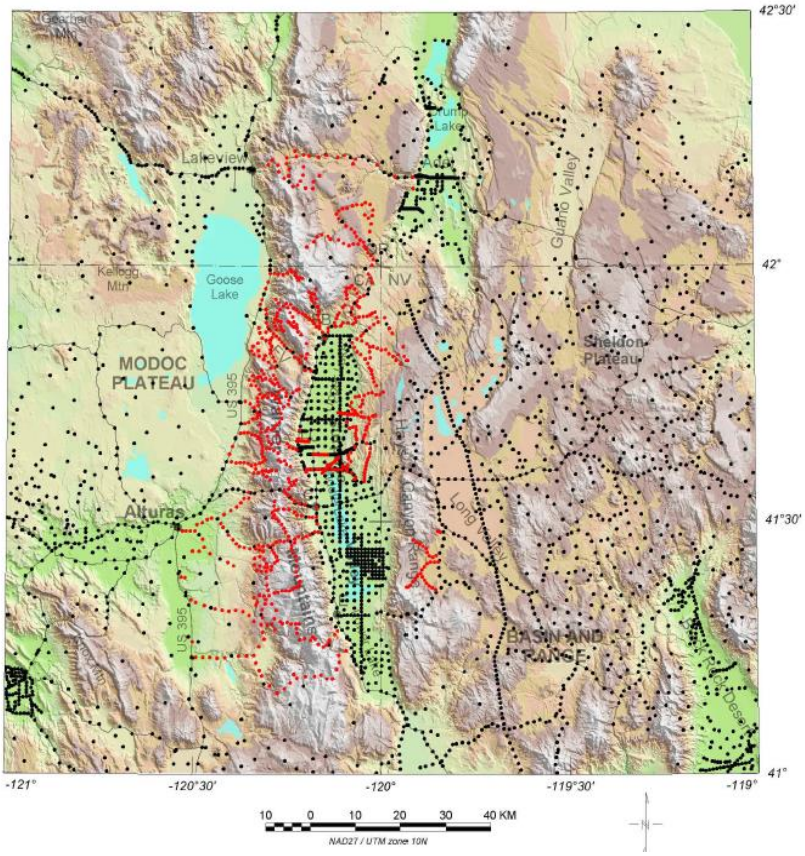


Credit: U.S. Geological Survey Department of the Interior/USGS
https://pubs.usgs.gov/of/2009/1157/of2009-1157.pdf

Figure 42: Topographic map of the area with observation points. The red dots indicate the location of the observation points from the previous studies, and black ones show the new gravity stations produced by USGS recently (after Egger et al., 2009).

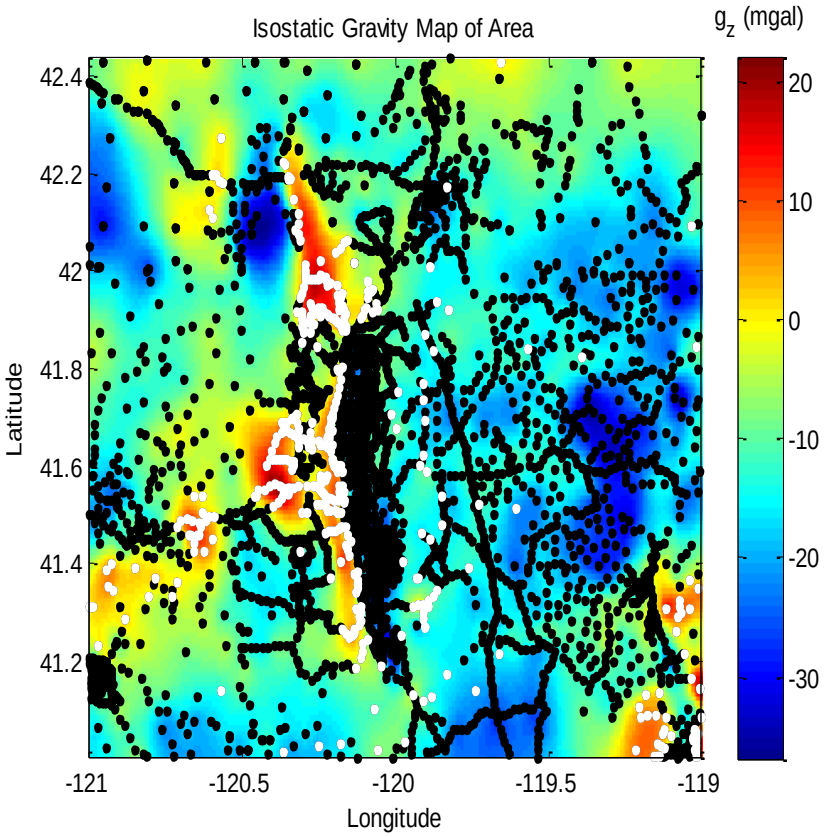


Figure 43: Map of the total isostatic gravity field in Surprise Valley. The black and white dots show the observation points, where white dots indicate the stations located at the basement outcrops.

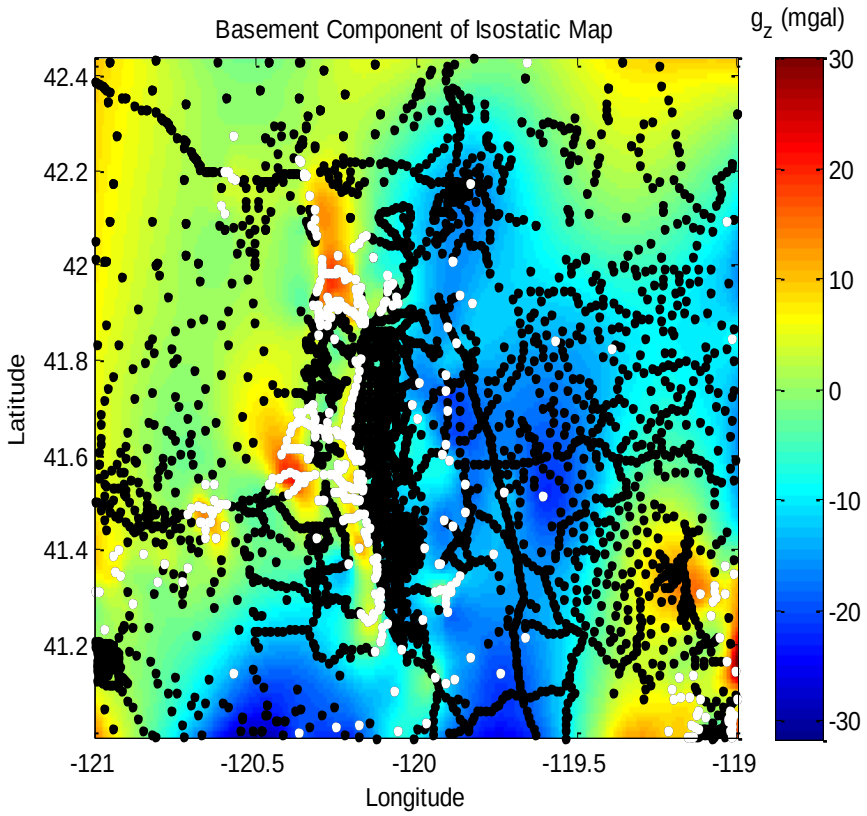


Figure 44: Map of the basement part isostatic gravity field in Surprise Valley. The black and white dots show the observation points, where white dots indicate the stations located at the basement outcrops.

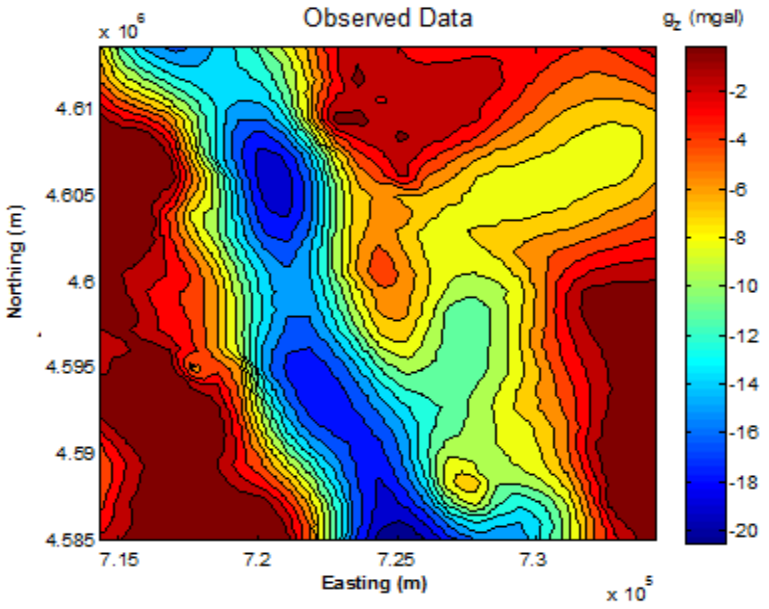


Figure 45: The map of the basin isostatic gravity field over the target area. The coordinates of the axis are given in meters.

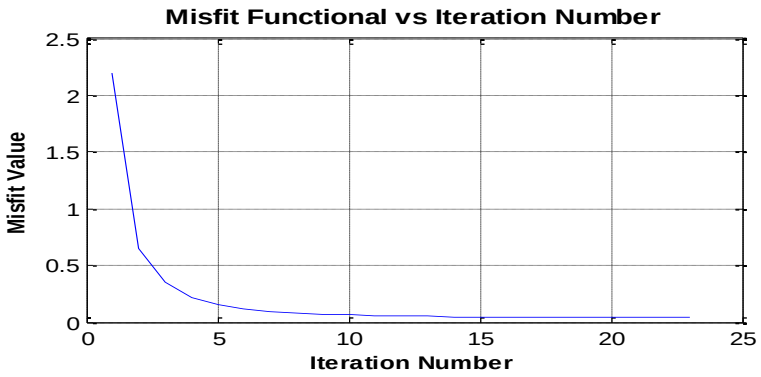


Figure 46: Plot of the relative misfit vs. the iteration number.

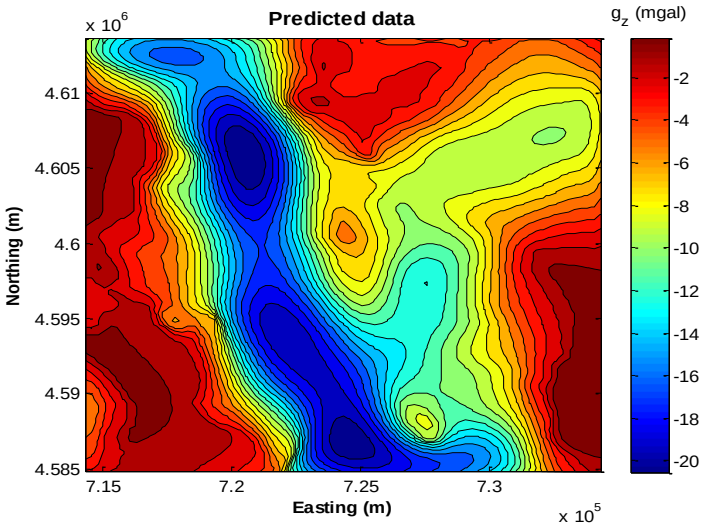


Figure 47: Map of predicted gravity data.

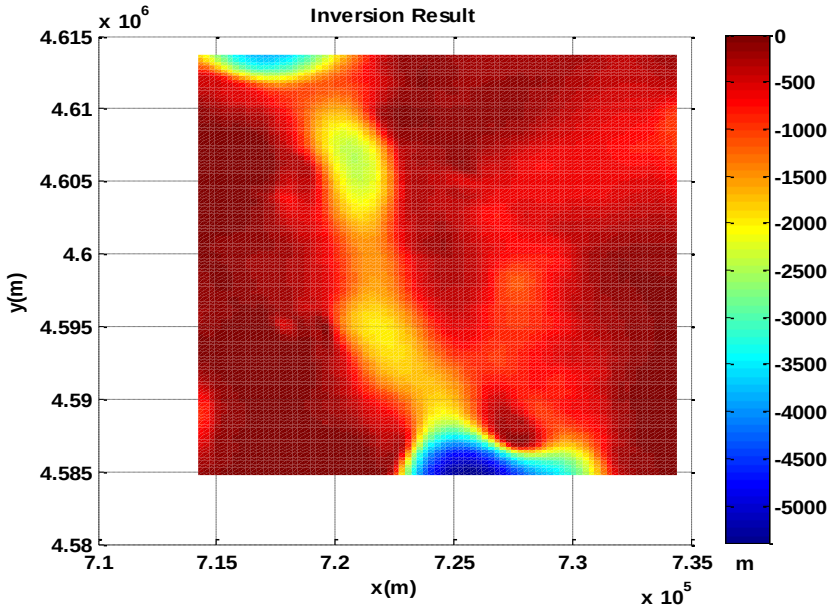


Figure 48: Map of the depth to the basement, obtained using the inversion method based on the Cauchy-type integral.

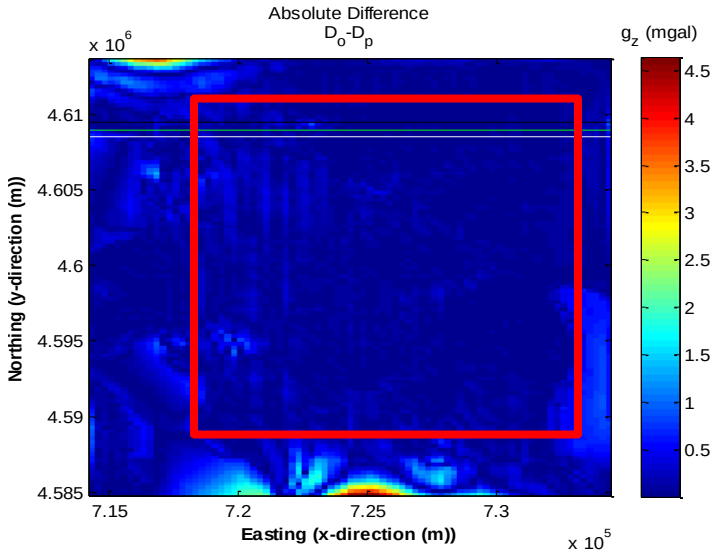


Figure 49: Map of absolute differences between the observed and predicted data. Red rectangle outlines the area with relatively low absolute differences.

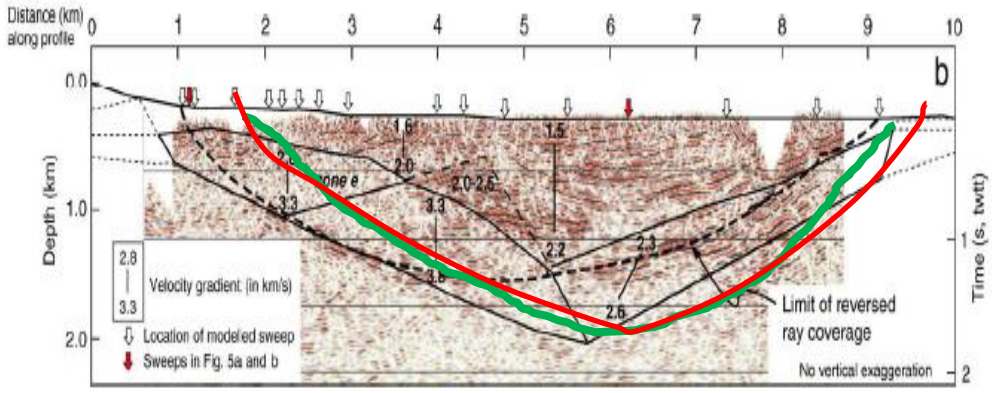


Figure 50: A seismic cross section along a profile. The dashed line shows the limit of the reversed ray coverage (after Egger et al., 2010). The red line represents the depth to the basement interpreted based on seismic data for this thesis. The green line shows the inversion result obtained using the depth-to-basement estimation based on the Cauchy-type integral.

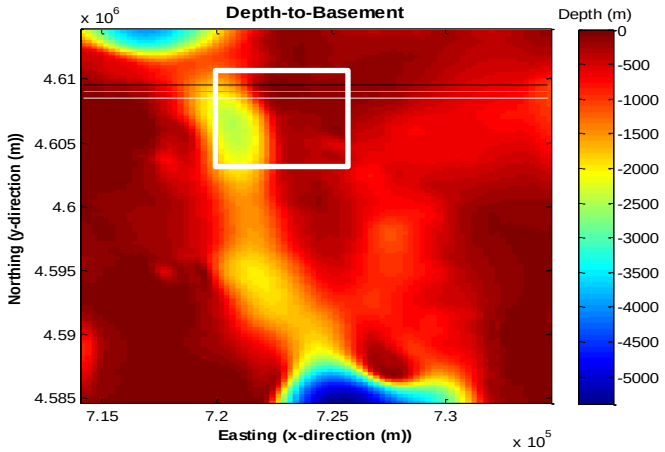


Figure 51: Map of the depth to the basement, obtained using the inversion method based on the Cauchy-type integral. Horizontal lines show three profiles taken along the x axis.

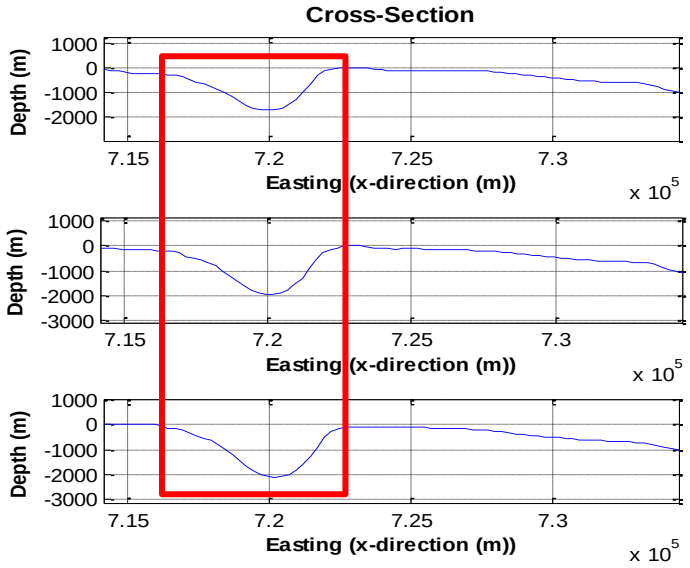


Figure 52: Vertical cross sections of the recovered depth to the basement taken along three profiles indicated by black, green, and white lines in Figure 52, respectively.

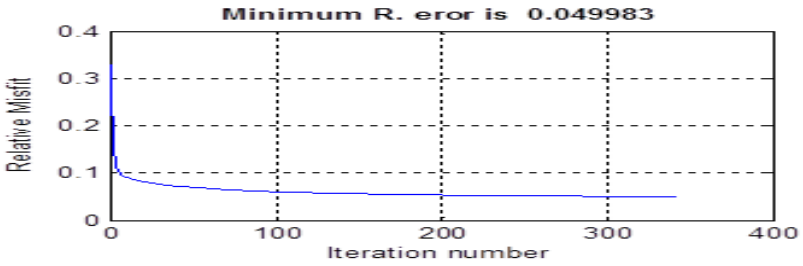


Figure 53: Plot of the relative misfit vs. the iteration number for the volume integral inversion.

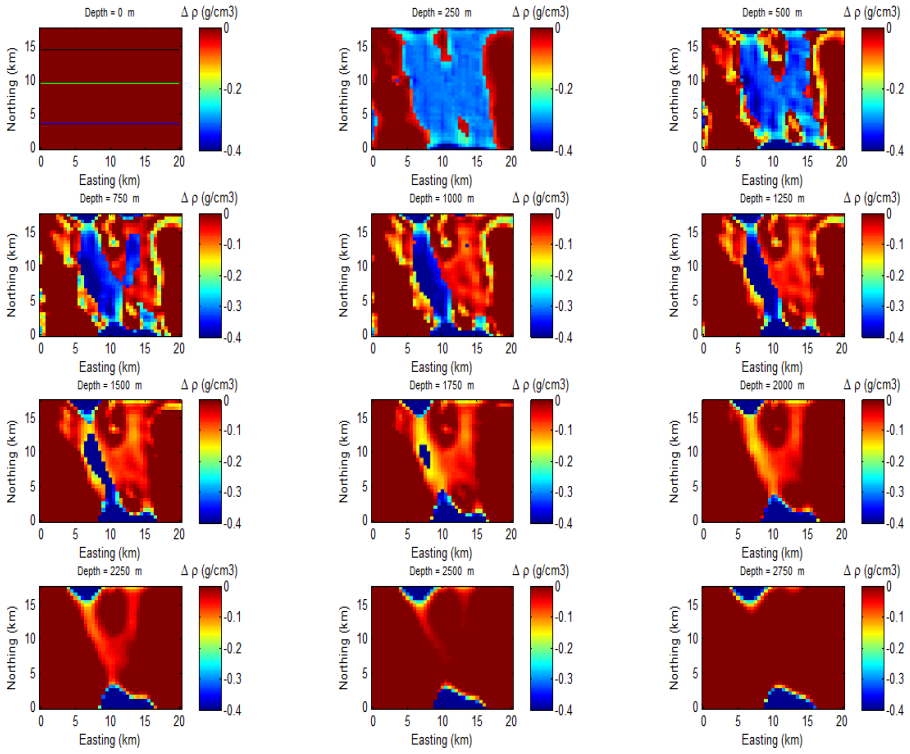


Figure 54: Horizontal sections at different depths of the inverse model obtained by the volume integral inversion.

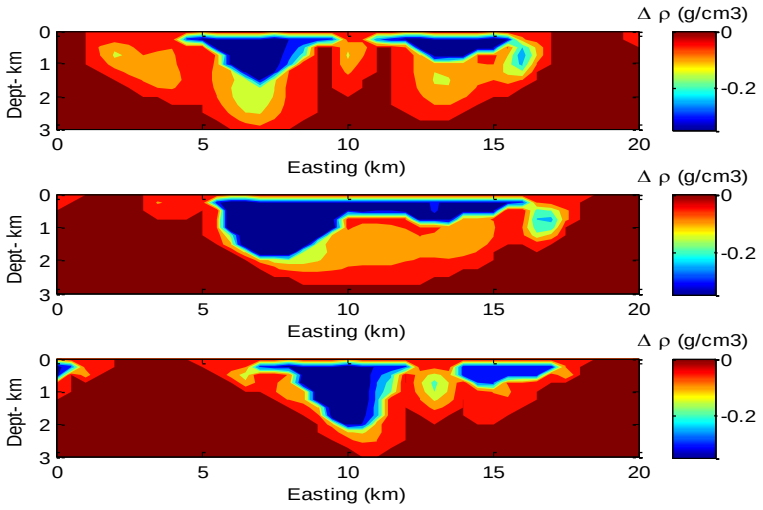


Figure 55: Vertical sections of the inverse model obtained by the volume integral inversion.

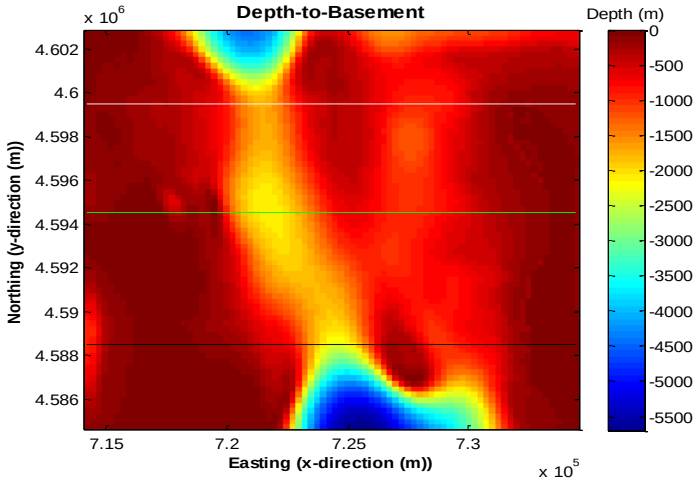


Figure 56: Map of the depth to the basement, obtained using the inversion method based on the Cauchy-type integral. The horizontal lines show three profiles used for a comparison.

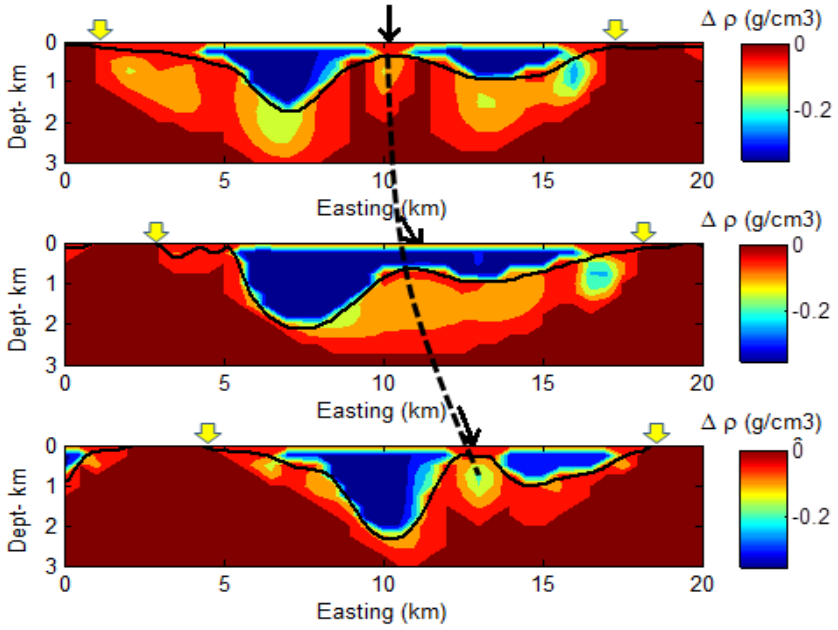


Figure 57: Vertical sections of the inverse density model produced by the volume integral method along three profiles shown in Figure 57. The yellow arrows indicate outcropping of the basement on the ground. The black arrows represent the orientation of possible faulting/basement relief. The solid black lines show the sediment-basement interface determined by the surface Cauchy-type integral method.

# CHAPTER 6

# CONCLUSION

I have developed the inversion algorithm and code for 3D inversion of the gravity data with the physical constrained and image focusing. In order to impose the constrained on the density distributions, I have applied the logarithmic space transformation with symmetric boundaries that are defined based on known geology. I have also applied focusing stabilizer to force the inversion to produce a more compact and focused results. The constrained and focusing inversion algorithm has been tested on variety of models, which demonstrated its efficiency.

I have also implemented the algorithm for the depth-to-basement estimation based on the surface Cauchy-type integral. This algorithm makes it possible to reduce the computational resources required for gravity inversion significantly.

I have tested this algorithm for different geological scenarios. It was demonstrated by the results of synthetic studies that the approach based on the Cauchy-type integral is capable of producing the results that are consistent with the true model of the sediment-basin interface. I have also tested the method on a model with poor data coverage in order to examine the performance of the

method in the situation, typical for real field data. It was shown that the method based on the Cauchy-type integral was able to recover the depth of sediment deposition for the models with the limited data coverage, but in this case, the termination criteria for misfit value must be adjusted accordingly to avoid producing the artificial effects.

Finally, I have used a real data set from USGS to invert for 3D depth of the basement and for the anomalous density distribution and compared the results with the published data. Both inversion algorithms applied to the observed gravity data produced a similar result consistent with known geology. However, the method based on the Cauchy-type surface integrals produced a clearer boundary between the sediments and the basements. At the same time, the method based on the volume integral was able to generate the image of the internal blocky structure of the basement.

Based on this study, I recommend a joint interpretation of the gravity data using both surface and volume integral approach because they may provide complimentary information about the subsurface geology from the observed gravity data.

# REFERENCES


Al-Zoubi, A., L. Eppelbaum, A. Abueladas, M. Ezersky, and E. Akkawi, 2013, Removing regional trends in microgravity in complex environments: Testing on 3D model and field investigations in the eastern Dead Sea Coast (Jordan): International Journal of Geophysics, 2013,1-13, doi: 10.1155/2013/341797.

Barbosa, V. C. F., and J. B. C. Silva, 1994, Generalized compact gravity inversion: Geophysics, 59, no. 1, 57-68.

Barbosa, V., J. Silva, and W. Medeiros, 1997, Gravity inversion of basement relief using approximate equality constrains on depths: Geophysics, 62, 1745-1757, doi: 10.1190/1.1444275.

Barbosa, V., J. Silva, and W. Medeiros, 1999a, Gravity inversion of discontinuous relief stabilized by weighted smoothness constrains on depths: Geophysics, 64, 1429-1437, doi: 10.1190/1.1444647.

Bonini, W. E., 1965, Bouguer gravity anomaly map of New Jersey: USGS, 9.

Bottrill, A. D., J. Van Hunen, and Allen, B. M., 2012, Insight into collusion zone dynamics from topography: Numerical modeling results and observations: Solid Earth, 3, 387-399, doi: 10.5194/se-3-387-2012

Cai H., and M. S. Zhdanov, 2014, Application of Cauchy-type integrals in developing effective methods for depth-to-basement inversion of gravity and gravity gradiometer data: Geophysics, 80, no. 2, 81-94, doi:10.1190/geo2014-0332.1

Cuma, M., G. A. Wilson, and M. S. Zhdanov, 2011, Large-scale 3D inversion of potential field data: Geophysical Prospecting, EAGE, 1-14, doi: 10.1111/j.1365-2478.2011.01052.x.

Egger, A. E., J. M. G. Glen, and D. K. McPhee, 2014, Structural controls on geothermal circulation in Surprise Valley, California: A re-evaluation of the Lake City fault zone, Geological Society of America Bulletin, B30785-1

Egger, A. E., J. M. G. Glen, D. A. Ponce, 2010, The northwestern margin of the Basin and Range province: Part 2- Structural setting of a developing basin from seismic and potential field data: Tectonophysics, 488, 150-161, doi:10.1016/j.tecto.2009.05.029.

Fan, J., Jiansheng, W., and Jialin W., 2008, Joint inversion of gravity and magnetic data for a two-layer model: Applied Geophysics, 5, no. 4, 331-339, doi: 10.1007/s11770-008-0042-2.

Fedi, M., and A. Rapolla, 1999, 3-D inversion of gravity and magnetic data with depth resolution: Geophysics, 64, no. 2, 452-460.

Glen, J. M. G., A. E. Egger, D. A. Ponce, 2008, Structures controlling geothermal circulation identified through gravity and magnetic transects, Surprise Valley, California, Northwestern Great Basin: GRC Transactions, Vol. 32

Ibarra, D. E., Egger, A. E., Maher, K., 2013, The late Pleistocene pluvial history of Surprise Valley, California, 26th Pacific Climate Workshop

Lerch, D. W., S. L. Klemperer, J. M. G. Glen, D. A. Ponce, E. L. Miller, and J. P. Colgan, 2009, Crustal structure of the northwestern Basin and Range Province and its transition to unextended volcanic plateaus: Journal of the Earth Science, 8, no.2, doi: 10.1029/2006GC001429

LaFehr, T. R., and M. N. Nabighian, 2012, Fundamentals of Gravity Exploration, Society of Exploration Geophysicists Geophysical Monograph Series Volume 17.

Last, J.B., and K. Kubik, 1983, Compact gravity inversion. Geophysics, 48, 713-721

Li, Y. and D. W. Oldenburg, 1998, 3D inversion of gravity data: Geophysics, 63, no. 1, 109-119.

Martins, C., W. Lima, V. Barbosa, and J. Silva, 2011a, Total variation regularization for depth-to-basement estimate: Part 1- Physicogeologic meaning and comparisons with previous inversion methods: Geophysics, 76, no. 1, I13-I20, doi: 10.1190/1.3524286.

Martins, C., V. Barbosa, and J. Silva, 2010, Simultaneous 3D depth-to-basement and density-contrast estimates using gravity data and depth control at few points: Geophysics, 75, no. 3, I21-I28, doi: 10.1190/1.3380225.

Martins, C., W. Lima, V. Barbosa, and J. Silva, 2011b, Total variation regularization for depth-to-basement estimate: Part 2- Mathematical details and applications: Geophysics, 76, no. 1, I1-I12, doi: 10.1190/1.3524286.

Ponce, D.A., Glen, J.M.G., Egger, A.E., Bouligand, Claire, Watt, J.T., and Morin, R.L., 2009, Geophysical studies in the vicinity of the Warner Mountains and Surprise Valley, northeast California, northwest Nevada, and southern Oregon: U.S. Geological Survey Open-File Report 2009-1157, 19 p., 6 data files. https://pubs.usgs.gov/of/2009/1157/of2009-1157.pdf

Portniaguine, O., and M. S. Zhdanov, 1999, Focusing geophysical inversion images: Geophysics, 64, no. 3, 874-887

Sawlan, M. G., and J. G. Frisken, 1989, Mineral Resources of the South Warner Contiguous Wilderness Study Area, Modoc County, California, USGS

Shamsipour, P., D. Marcotte, and M. Chouteau, 2012, 3D stochastic joint inversion of gravity and magnetic data: Journal of Applied Geophysics, 79, 27-37, doi:10.1016/j.jappgeo.2011.12.012

Silva, J., D. Costa, and V. Barbosa, 2006, Gravity inversion of basement relief and estimation of density contrast variation with depth: Geophysics, 71, no. 5, J51-J58, doi: 10.1190/1.2236383.

Silva, J., W. Medeiros, and V. Barbosa, 2001, Potential field inversion: Choosing the appropriate technique to solve a geologic problem: Geophysics, 66, 511-520, doi: 10.1190/1.1444941.

Silva, J., A. Oliviera, and V. Barbosa, 2010a, Gravity inversion of 2D basement relief usingentropic regularization: Geophysics, 75, no.3, I29-I35, doi: 10.1190/1.3374358.

Silva, J., F. Oliviera, V. Barbosa, and H. Campos Velho, 2007, Apparent-density mapping using entropic regularization: Geophysics, 72, no.4, I51-I60, doi: 10.1190/1.2732557.

Silva, J., S. Vasconcelos, and, V. Barbosa, 2007, Apparent-magnetization mapping using entropic regularization: Geophysics, 75, no.2, L 39-L50, doi: 10.1190/1.3358160.

Tikhonov, A. N., and V. Y. Arsenin, 1977, Solution of ill-posed problems: V. H. Winston & Sons.

Zhdanov, M, S., 1980, Use of Cauchy integral analogs in the geopotential field theory: Annales de Geophysique, 36, 447-458.

Zhdanov, M, S., 1984, Cauchy integral analogs in the geophysical field theory (in Russian): Nauka.

Zhdanov, M, S., 1988, integral transforms in geophysics: Springer-Verlag.

Zhdanov, M. S., 2002, Geophysical inverse theory and regularization problems: Elsevier.

Zhdanov, M. S., 2009, Geophysical Electromagnetic Theory and Methods: Elsevier, 310-313 pp.

Zhdanov, M. S., A. V. Gribenko, and G. A. Wilson, 2012, Generalized joint inversion of multimodal geophysical data using Gramian constraints: Geophysical Research Letters, 39, no. 9, L09301, doi: 10.1029/2012GL051233.

Zhdanov, M. S., and E. Tolstaya (2004), Minimum support nonlinear parametrization in the solution of a 3D magnetotelluric inverse problem, Inverse Probl., 20, no. 3, 937-952, doi:10.1088/0266-5611/20/3/017

Zhdanov, M. S., and H. Cai, 2013, Inversion of gravity and gradiometry data for density contrast surfaces using Cauchy-type integrals: 83rd Annual International Meeting, SEG, Expanded Abstracts, 1161-1165.

Zhdanov, M, S., and X. Lui, 2013, Cauchy-type integrals for terrain correction of gravity and gradiometry data: Geophysical Journal International, 194, 294-268, doi: 10.1093/gji/ggt120

Zhdanov, M, S., and H. Cai, 2015, Application of Cauchy-type integrals in developing effective methods for depth-to-basement inversion of gravity and gradiometry data: Geophysics, 80, 1-14, doi: 10.1190/GEO2014-0332.1.

Zhu, Y., M. S. Zhdanov, and M. Čuma, 2013, Gramian constraints in the joint inversion of airborne gravity gradiometry and magnetic data: SEG Houston 2013 Annual Meeting, 1166-1170, http://dx.doi.org/10.1190/segam2013-0735.1